Research

A study of the photocatalytic and photothermal properties of the quaternary rGO/TiO₂/NiFe₂O₄/ZnO nanocomposite for water treatment

Ahmad Faig Amin¹ · Mahmood Rezaee Roknabadi¹ · Mohammad Behdani¹ · Mohammad Ranjbar¹

Received: 16 December 2024 / Accepted: 9 May 2025

Published online: 21 May 2025 © The Author(s) 2025 OPEN

Abstract

This study presents the synthesis and evaluation of a novel rGO/TiO2/NiFe2O4/ZnO nanocomposite for efficient solar steam generation (DSSG) and photocatalytic water purification. The nanocomposite, synthesized via a hydrothermal method, demonstrates exceptional photothermal performance, achieving a maximum evaporation rate of 3.53 kg m $^{-2}$ h $^{-1}$ and an evaporation efficiency of 89% under 3 sun illumination. The incorporation of reduced graphene oxide (rGO) facilitated effective heat localization at the water/air interface, minimizing heat loss to the bulk water, as confirmed by infrared imaging and temperature sensor data. Furthermore, the nanocomposite exhibited significant photocatalytic activity, effectively degrading methylene blue with a degradation efficiency of 97%. Water quality analysis confirmed the production of clean and drinkable water. The nanocomposite demonstrated excellent reusability and stability across multiple cycles. This cost-effective and efficient material holds significant potential for sustainable water purification and solar steam generation applications.

Keywords Clean water production · Interfacial evaporation · Photothermal material · Photocatalytic · Photoabsorber

1 Introduction

Water, which covers over 70% of the Earth's surface, gives our planet its characteristic blue appearance from space. However, this apparent abundance masks a critical scarcity of potable water. The vast majority of Earth's water is saline and unsuitable for consumption, and the compounding effects of climate change, population growth, and increasing pollution have intensified this problem in recent decades, leading to severe water shortages globally. Many regions, particularly in Africa and parts of Asia, lack access to clean water. A United Nations World Water Development Report [1] projects that by 2050, 748 million people will face drinking water scarcity.

The vast quantities of water in oceans, seas, and rivers are largely unusable for direct consumption due to salinity levels. Desalination and wastewater treatment offer potential solutions to mitigate these shortages and avert a global crisis. Techniques such as reverse osmosis [2–4], electrocoagulation [5], membrane filtration [6, 7], thermal-based methods [8, 9], and hybrid thermal-membrane processes like membrane distillation [10, 11] have been developed for this purpose. However, these methods often suffer from limitations, including low efficiency, high costs, reliance on non-renewable energy sources, operational complexity, and the emission of greenhouse gases, particularly carbon dioxide [9, 12, 13].

Mahmood Rezaee Roknabadi, roknabad@um.ac.ir | ¹Department of physics, Faculty of Science, Ferdowsi University of Mashhad, Mashhad, Iran.



Discover Materials

(2025) 5:83

| https://doi.org/10.1007/s43939-025-00266-y



Discover Materials

These drawbacks impede the widespread and sustainable application of these techniques as long-term solutions to the global water crisis.

To effectively address the clean water shortage, we must draw inspiration from nature. The water cycle, a solar-powered process, naturally converts billions of liters of saline water into potable water daily, culminating in rainfall. In recent years, there has been a significant shift towards replacing conventional desalination techniques with greener, more environmentally friendly approaches that harness solar energy. Photothermal conversion, which utilizes light to generate heat, has emerged as a promising sustainable energy source for solar desalination. Researchers have explored diverse photothermal materials to produce clean drinking water from various sources, including wastewater, saline water [14–19], and even atmospheric moisture [20]. Direct solar steam generation (DSSG) systems, which employ nanocomposites with combined light-absorbing and heat-transfer capabilities to evaporate water and produce clean distillate, represent a particularly promising technology for mitigating water scarcity.

Reduced graphene oxide (rGO), with its high surface area, offers excellent adsorption capacity for water molecules, enhancing water molecules capture during distillation. The desirable optical properties of graphene-based materials have led to the widespread use of these materials in photothermal evaporation [21-24]. TiO₂, a well-established photocatalyst, efficiently utilizes light energy to generate reactive oxygen species (ROS) capable of degrading organic pollutants and inactivating bacteria in water. Similarly, ZnO exhibits strong photocatalytic activity and can be activated by visible light, reducing reliance on ultraviolet light [25, 26]. However, the high recombination rate of photogenerated excitons in both TiO_2 and ZnO can limit the nanostructures photocatalytic performance. Nickel ferrite (NiFe₂O₄), a metal ferrite, offers good chemical stability, low conductivity, catalytic performance, and antibacterial properties [27–29], making it a valuable component in DSSG systems. Furthermore, the magnetic properties of NiFe₂O₄ facilitate material recovery and removal from treated water using an external magnetic field, a crucial aspect of sustainable water treatment.

Combining multiple materials into nanocomposites is a common strategy to enhance desired properties and mitigate undesirable ones. Numerous studies have investigated the photocatalytic properties of rGO-TiO₂ nanocomposites [30], demonstrating promise in applications such as volatile organic compound removal [31], antibacterial water treatment [32], and contaminant degradation [33–35]. Similarly, rGO-ZnO nanocomposites have shown excellent photocatalytic properties due to increased electron-hole charge transfer [36–39]. Researchers have also utilized ZnO-rGO composites for dye removal, leveraging the electronic properties of rGO to suppress electron-hole recombination in ZnO and enhance its photocatalytic activity [39]. ZnO-decorated TiO₂-rGO nanocomposites have also demonstrated potential for organic dye removal from water [40]. NiFe₂ O_4 , which possesses photocatalytic properties, has been used in hydrogen generation through water splitting [41]. BiVO₄/NiFe₂O₄ composites have been reported as efficient photocatalysts for polluted water detoxification [42]. Kalita et al. reported a green synthesis of magnetically separable NiFe₂O₄/rGO nanocomposites with promising photocatalytic properties for methylene blue and methyl orange removal, demonstrating successful recovery and reuse using a magnetic field [43].

Building upon our previous investigations of rGO-TiO₂-NiFe₂O₄ nanocomposites, which demonstrated promising antibacterial and photocatalytic properties under UV and visible light irradiation [44], we aimed to explore the potential of a more complex quaternary nanocomposite for advanced applications. Ternary nanocomposites consisting of similar components have been explored in previous studies, showing potential application in photocatalysis. For instance, Abdi et al. [45] synthesized ZnO-covered NiFe₂O₄ nanospheres on N-doped rGO nanosheets, achieving 93% methylene blue (MB) degradation in 240 min. Similarly, Atashi et al. [46] reported excellent photocatalytic reusability for rGO/TiO₂/ NiFe₂O₄. However, a significant gap remains in the literature: neither of these studies explored the application of these nanocomposites in a Direct Solar Steam Generation (DSSG) system, an area of critical importance for addressing global water scarcity.

Therefore, in this work, we present the synthesis of a novel quaternary nanocomposite, rGO-TiO₂-NiFe₂O₄-ZnO, as a new photocatalyst specifically designed for application in a DSSG system, utilizing a hydrothermal technique. To the best of our knowledge, this is the first study to utilize a nanocomposite composed of rGO, TiO2, NiFe2O4, and ZnO for DSSG applications. This unique combination of four components offers potential synergistic effects that are not achievable with ternary composites, presenting a novel approach to enhancing solar steam generation.

By combining the photocatalytic properties of the individual components with the high specific surface area of graphene and the magnetic nature of nickel ferrite, we aim to achieve enhanced photocatalytic activity and facile recyclability of the synthesized nanocomposite for water treatment in closed systems. While we recognize the potential for magnetic separation of the nanocomposite from treated water, as demonstrated in NiFe₂O₄/rGO [43] and ZnO/NiFe₂O₄/ rGO [45] nanocomposites, this aspect is not the primary focus of our current study. Instead, we concentrate on the



synergistic enhancement of photocatalytic and DSSG performance through the unique quaternary composition and systematic optimization of the rGO concentration.

We have conducted a systematic optimization of the rGO concentration within the nanocomposite, maintaining constant masses for the other components. By varying the graphene oxide (GO) mass from 1 to 5 times, in the quaternary nanocomposite synthesis process, relative to the other components, we have identified the optimal GO concentration for both photocatalytic and DSSG applications. This systematic approach to optimization is a key contribution of our research.

The structural and morphological properties of the synthesized nanocomposites were investigated using X-ray diffraction (XRD) pattern, field-emission scanning electron microscopy (FESEM), and energy-dispersive X-ray spectroscopy (EDX). The photocatalytic properties of the synthesized nanocomposites were evaluated by monitoring methylene blue (MB) degradation under UV light irradiation. The best-performing photocatalyst was then incorporated into a custom-built DSSG setup, and its evaporation rate and evaporation efficiency were examined. Inductively coupled plasma optical emission spectrometry (ICP-OES) was used to analyze the concentration of sodium, potassium, magnesium, and calcium ions in the produced water by condensing the vaporized water, and the pH of both the saline water and the produced water was measured. Finally, the light-to-heat conversion and heat localization properties of the nanocomposite were characterized using infrared (IR) imaging. Durability and stability of the nanocomposite were explored by cycling of methylene blue degradation for five consecutive cycles and XRD analysis of the collected powder after methylene blue degradation.

2 Materials and method

2.1 Preparation of GO

Graphene oxide (GO) was synthesized using a modified Hummers'method [47]. In this procedure, 80 mmol of graphite powder was added to a mixture of phosphoric acid, nitric acid, and sulfuric acid. The volumetric ratio of these acids was 10:22.5:67.5, respectively. The mixture was cooled in an ice bath. Then, 40 mmol of potassium permanganate was slowly added. The resulting solution was stirred for 2 h at 50 °C. Subsequently, the temperature was increased to 85 °C, and 100 mL of deionized (DI) water was added. After stirring for 1 h, an additional 120 mL of DI water was added. This was followed by the dropwise addition of 15 mL of hydrogen peroxide (H_2O_2). This addition caused a color change from dark brown to yellow. Excess metal ions were removed by filtration and washing with a 1:10 aqueous solution of hydrochloric acid (HCI). Unexfoliated graphite particles were separated by centrifugation at 750 rpm. Once the pH of the solution reached 6–7, the solution was centrifuged at 8000 rpm. The resulting precipitate was washed repeatedly with DI water. Finally, the remaining powder was dried overnight at room temperature.

2.2 Synthesis of TiO₂ nanoparticles

 ${
m TiO}_2$ nanoparticles were synthesized via a sol–gel method. Titanium(IV) isopropoxide (TTIP, Merck, 99%) and polyvinylpyrrolidone (PVP 40000, Sigma Aldrich) were combined. The stoichiometric ratio was 0.002 mol TTIP to 0.4 mol PVP in 50 mL of ethanol. This solution was stirred for 10 min to ensure homogeneity. A 1 M NaOH solution was then added dropwise. This addition continued until the solution became opaque. The opacity indicated the formation of ${
m TiO}_2$ nanoparticles. The resulting precipitate was isolated by centrifugation. It was then dried at 50 °C. Finally, the precipitate was calcined at 400 °C for 2 h.

2.3 Synthesis of NiFe₂O₄ powder

NiFe $_2$ O $_4$ nanoparticles were synthesized using a hydrothermally assisted co-precipitation method, as described previously [44]. Briefly, a stoichiometric mixture of 0.02 mol FeCl $_3$ ·6H $_2$ O (Sigma Aldrich, 99%) and 0.01 mol NiCl $_2$ ·6H $_2$ O (Sigma Aldrich, 99%) was dissolved in 100 mL of deionized (DI) water. This solution was refluxed at 80 °C for 30 min. Subsequently, 10 mL of ammonium hydroxide was added. The mixture was then refluxed for an additional 3 h at 80 °C. The resulting precursor was transferred to a stainless-steel autoclave. Hydrothermal treatment was then performed at 180 °C for 8 h. The final NiFe $_2$ O $_4$ nanoparticles were isolated. This isolation involved repeated washing with ethanol and DI water. Finally, the nanoparticles were dried in an oven at 50 °C for 12 h.



2.4 Synthesis of ZnO nanoparticles

ZnO nanoparticles were synthesized using a hydrothermal method. Zinc nitrate, citric acid (as a complexing agent), deionized water, and ethanol were used in the synthesis [48]. Initially, zinc nitrate ($Zn(NO_3)_2 \cdot 6H_2O$) was dissolved in a mixture of 100 mL of deionized water and ethanol. The concentration was 0.1 mol. This solution was stirred for 30 min at 40 °C. Citric acid was then added gradually. This continued until it was completely dissolved. No particles were visible in the solution. Subsequently, the solution was placed in a hydrothermal reactor. It was heated at 120 °C for 8 h. A dry, fluffy gel was obtained. To ensure complete drying, the gel was heated at 100 °C for 1.5 h. This resulted in a dried gel. The dried gel was then ground. The resulting fine powder was calcined in a furnace at 500 °C for 2 h under a nitrogen-free atmosphere.

2.5 Synthesis of GTNZ nanocomposite

This study investigated the photocatalytic activity and solar water evaporation performance of $rGO/TiO_2/NiFe_2O_4/TiO_3$ and composites. To examine the effect of rGO concentration on the composite's photocatalytic and distillation efficiency, five samples were prepared varying rGO content to other components from 1:1 to 5:1.

For the synthesis of a typical sample with a $rGO:TiO_2:NiFe_2O_4:ZnO$ weight ratio of 1:1:1:1, 50 mg of graphene oxide (GO) was dispersed in 50 mL of deionized (DI) water. This dispersion was achieved using a horn sonicator at 25 kHz. Separately, 50 mg each of titanium dioxide (TiO_2), nickel ferrite ($NiFe_2O_4$), and zinc oxide (ZnO) nanoparticles were dispersed in 100 mL of DI water. The same sonication method was used. Both solutions were sonicated for 15 min. Then, 1 g of sodium hydroxide (NaOH) was added to the TiO_2 -containing solution. This served as a source of hydroxide ions. It also adjusted the solution's pH and facilitated the partial reduction of GO to reduced graphene oxide (rGO) during subsequent hydrothermal treatment. Following the addition of NaOH, the solution was stirred for an additional hour.

The resulting solution was then added dropwise to the GO solution. This occurred under simultaneous stirring and sonication. The combined 150 mL solution was transferred to a 200 mL Teflon-lined stainless steel autoclave. It was then heated at 100 °C for 18 h. Figure 1 shows a schematic diagram for the GTNZ nanocomposite synthesis procedure.

After the heating period, the resulting powder formed a soft tablet at the bottom of the autoclave. 100 mL of the supernatant liquid was carefully removed with a syringe. Then, 100 mL of DI water was added to the remaining material. This mixture was centrifuged and washed repeatedly with DI water. Washing continued until the pH reached 7. The final product was dried at 60 °C for 12 h in an oven after centrifugation.

The same procedure was followed for the other samples. These samples had different weight ratios of rGO to the other components. Samples with rGO:TiO₂:NiFe₂O₄:ZnO weight ratios of 2:1:1:1, 3:1:1:1, 4:1:1:1, and 5:1:1:1 were

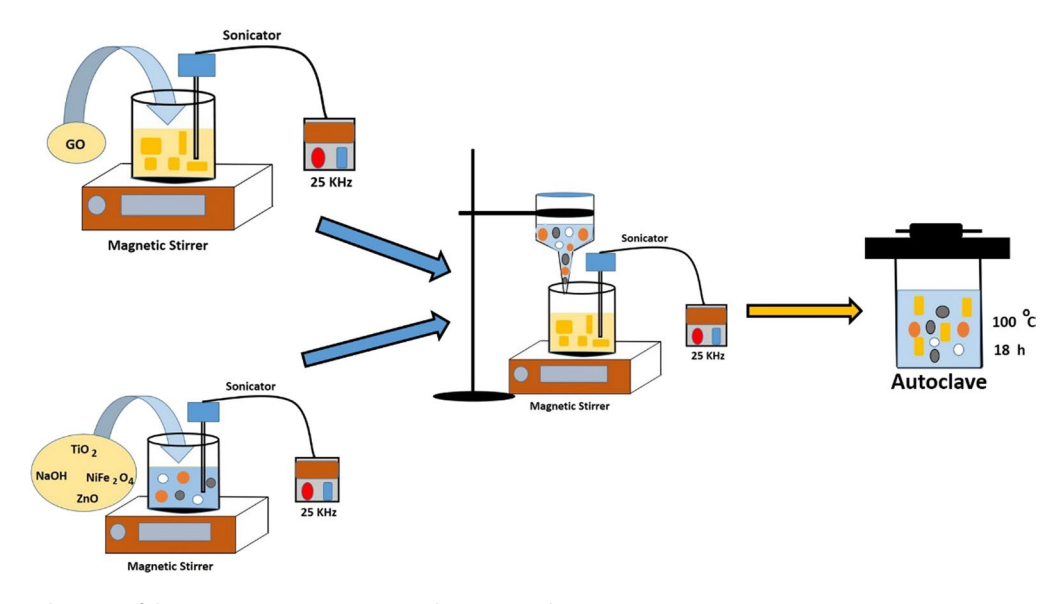


Fig. 1 Schematic diagram of the GTNZ nanocomposite synthesis procedure



Sample	Weight ratio	rGO (mg)	TiO ₂ (mg)	ZnO (mg)	NiFe ₂ O ₄ (mg)
GTNZ 11	1:1:1:1	50	50	50	50
GTNZ 21	2:1:1:1	100	50	50	50
GTNZ 31	3:1:1:1	150	50	50	50
GTNZ 41	4:1:1:1	200	50	50	50
GTNZ 51	5:1:1:1	250	50	50	50

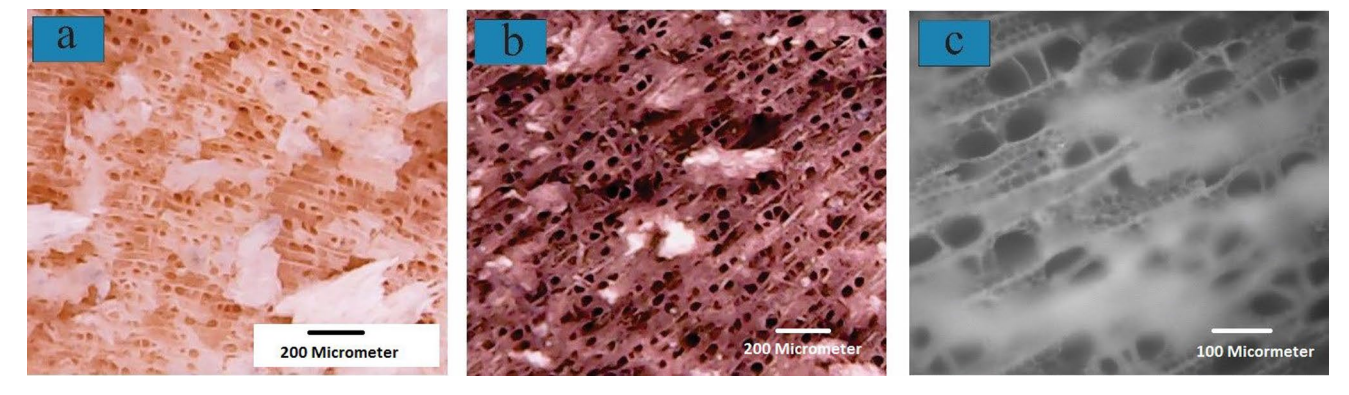


Fig. 2 a, b Optical microscope image of poplar wood before and after coated with nanocomposite at $100 \times \text{magnification}$ and c optical microscope image of the photoabsorber coated with nanocomposite at $200 \times \text{magnification}$

prepared. These samples were designated GTNZ 21, GTNZ 31, GTNZ 41, and GTNZ 51, respectively. Table 1 summarizes the details of the different sample preparation conditions.

2.6 Sample preparation for photocatalytic analysis

(2025) 5:83

To determine the photocatalytic ability of the prepared nanocomposites, the photodegradation of methylene blue (MB) solution under UV light was evaluated. This evaluation was performed by analyzing the absorption spectrum of samples at different UV light exposure times. To prepare the solution for photocatalysis characterization, 3.2 mg of nanocomposite was dispersed in 50 mL of a 20 ppm MB solution. The MB solution was pre-dissolved in DI water. The solution was kept under constant stirring for 30 min in the dark. Then, the solution was exposed to a 200 W HBO Mercury lamp. The light source had an intensity of 50 mW cm⁻². Samples were taken every 15 min. The absorption spectrum of these samples was then recorded using UV/visible spectroscopy.

2.7 Sample preparation for DSSG experiment

The sample exhibiting the best optical properties, including optimal optical absorbance and photocatalytic performance—GTNZ 41—was selected for the Direct Solar Steam Generation (DSSG) experiment. For this experiment, a specific amount of nanocomposite was dispersed in 10 mL of DI water to create a suspension, serving as the photoabsorber. To minimize heat loss to the bulk water, poplar wood substrates, with a 40 mm diameter and 10 mm thickness, were used.

Poplar wood was chosen due to its exceptional water transport capabilities. Its natural vascular structure comprises two distinct conduit types: large-diameter vessels (greater than $60 \mu m$) and smaller-diameter tracheids (less than $20 \mu m$). These conduits are interconnected by pits, enabling efficient lateral water flow. This interconnected network makes poplar wood an ideal substrate for DSSG systems. It ensures continuous water replenishment to the photoabsorber surface, even when channel blockage occurs due to salt precipitation or particulate contamination. Optical microscopy images of the substrate surface, both before and after nanocomposite coating, are shown in Fig. 2. Notably, the coating process does not obstruct the microchannels, preserving the accessibility of both vessel and tracheid lumens, thereby maintaining the substrate's water transport functionality.

These substrates were washed with DI water for 15 min in an ultrasonic bath and dried in an oven at 60 °C for 4 h. To prepare the photo absorber, 10 mL suspension of GTNZ 41 nanocomposite with different concentration was dropped



cast on the substrates on hot plate. A solar simulator with 750 W xenon lamp with filters to correct wavelengths was used as an artificial solar irradiance. The DSSG aperture includes a 100 mL beaker for saline water, with 3 temperature sensors at 2, 3 and 4 cm from the bottom of the beaker to record the temperature at different distances from the surface of the water which the light irradiates. We used a precise digital scale to record the mass of the beaker containing seawater in order to calculate evaporation rate, \dot{m} , using Eq. (1):

$$\dot{m} = \frac{\Delta m}{A \Delta T} \tag{1}$$

where Δm is the mass reduction differences of the seawater in the DSSG process in light and dark, as below:

$$\Delta m = \Delta m_{light} - \Delta m_{dark} \tag{2}$$

Which in this relation Δm_{light} is the mass reduction during DSSG experiment while light is on and Δm_{dark} is the mass reduction of seawater in the same DSSG experiment condition while the light is off.

A is the area of photoabsorber and ΔT is the time of the DSSG test. The evaporation efficiency of the photoabsorber was calculated using Eq. (3):

$$\eta = \frac{\dot{m}h_{LV}}{C_{Opt}q_i} \tag{3}$$

where \dot{m} represents the evaporation rate, h_{LV} is the total enthalpy of vaporization, C_{Opt} is the optical concentration and q_i , represents the normal incoming solar intensity [49].

We prepared five samples with different concentrations from nanocomposite GTNZ 41 as photoabsorber in order to coat poplar wood surface and evaluate the photoabsorbers steam generation performance under simulated solar light irradiation. The nanocomposite concentration varies from 1.5 to 3, 4.5, 6 and 7.5 g L^{-1} for photoabsorbers which we name them S1, S2, S3, S4 and S5 here in after. The nanocomposite suspension was dropped cast on the washed poplar wood on the heat plate at 60 °C slowly until 10 mL solution was finished. Figure 3 shows a schematic diagram of the DSSG system for generating water vapor from illuminated simulated sunlight.

2.8 Optical band gap determination

The optical band gap energies (E_g) of the synthesized materials were determined using Tauc plots, derived from UV–Vis absorption spectra. The Tauc relation is given by the equation below:

$$(\alpha h v)^n = A(h v - E_a) \tag{4}$$

where α is the absorption coefficient, hv is the photon energy, A is a constant, E_g is the band gap energy, and n is a factor that depends on the transition type (n = 1/2 for direct transitions). By plotting $(\alpha hv)^n$ against hv and extrapolating the linear portion of the plot to the hv axis, the band gap energy (E_n) was determined [50].

2.9 Valence and conduction band position estimation

To estimate the valence band (VB) and conduction band (CB) positions, the Butler-Ginley equations were employed. These equations relate the band edge potentials to the band gap energy (E_g) and the absolute electronegativity (χ) of the semiconductor materials:

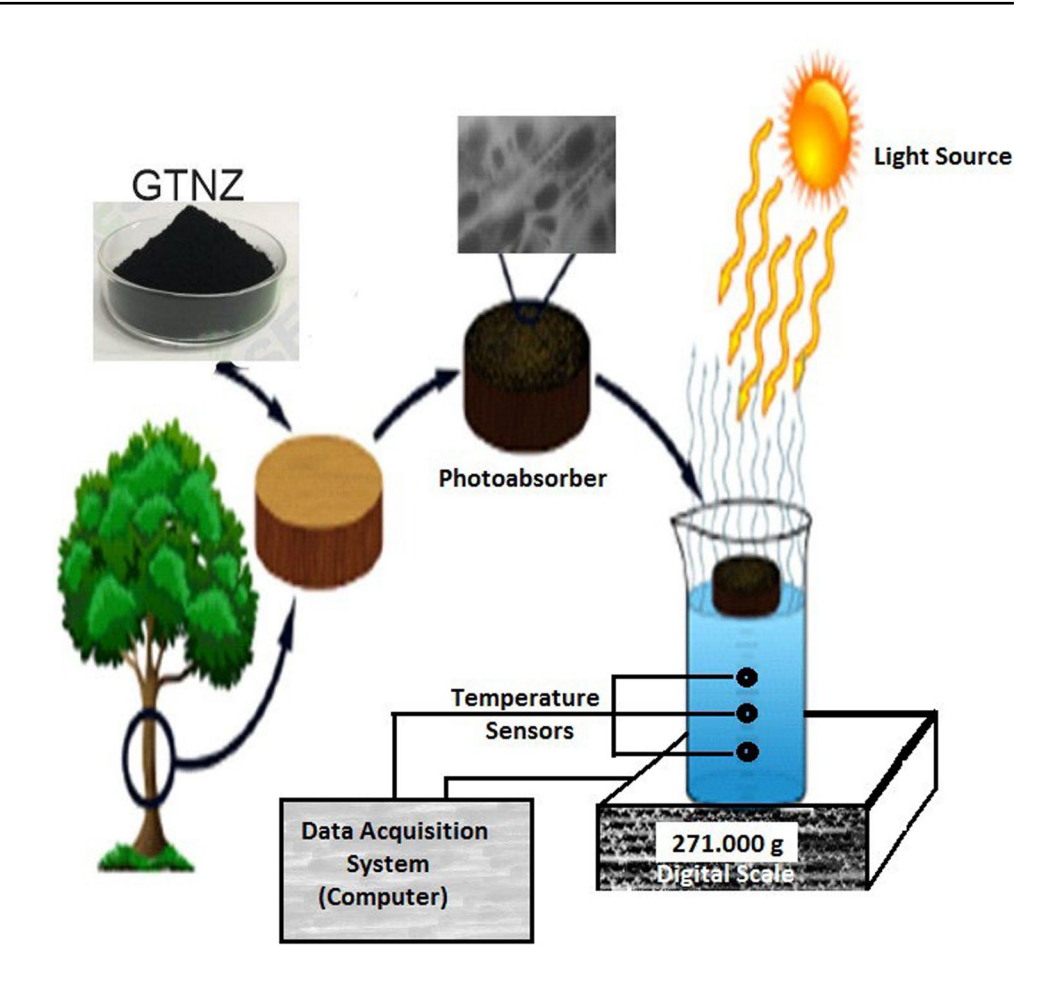
$$E_{VB} = \chi - E_e + 0.5E_g \tag{5}$$

$$E_{CB} = E_{VB} - E_q \tag{6}$$

where E_{VB} and E_{CB} are the valence and conduction band edge potentials, respectively, χ is the absolute electronegativity of the semiconductor, E_e is the energy of free electrons on the hydrogen scale (approximately 4.5 eV), and E_g is the band gap energy determined from the Tauc plots [51, 52].



Fig. 3 A simple schematic diagram of the DSSG experiment using poplar wood as the substrate and GTNZ 41 nanocomposite at the waterair interface



2.10 Instrumentation

Photocatalytic activity measurement: The photocatalytic activity of the nanocomposites and UV-visible spectroscopy data were recorded using a UV-Visible system (UVD 2950).

Phase analysis: The structural properties of the synthesized nanocomposites were investigated using X-ray diffraction (XRD) on a (D8 Advance Bruker YT model, Cu Kα radiation) system.

Morphology and composition analysis: Energy-dispersive X-ray spectroscopy (EDX) and field-emission scanning electron microscopy (FE-SEM) images were obtained using a TESCAN-XMO device.

pH measurement: The pH of the solutions was measured using a pH meter (Model AZ 86502).

Electrical conductivity measurement: The electrical conductivity of seawater before and after desalination was measured using an LCR meter (Model GPS-313813, UK).

Desalination performance: Concentration of four ions (Na⁺, K⁺, Ca²⁺ and Mg²⁺) of the seawater before and after DSSG experiment were measured using ICP-OES technique, Spectro Arcos-76004555 plasma, AMETEK (ARCOS FHE12).

Characterization and measurements: The structural and morphological properties of the synthesized GTNZ composites were investigated using X-ray diffraction (XRD) and field-emission scanning electron microscopy (FESEM), respectively. Photocatalytic activity was assessed by evaluating the nanocomposites'ability to degrade methylene blue (MB) under UV light irradiation, monitoring the solution's absorbance.

The interfacial vapor generation rate of the synthesized samples was measured using a solar simulator equipped with a precision balance and a temperature monitoring system. Brunauer–Emmett–Teller (BET) and Barrett-Joyner-Halenda (BJH) analyses were used to determine the specific surface area and pore size distribution of the photo-thermal nanocomposites.

Inductively coupled plasma optical emission spectrometry (ICP-OES) was used to determine the concentration of sodium, potassium, magnesium, and calcium ions in the distilled water. The quality of the condensed water was



Discover Materials

evaluated by measuring its pH and conductivity, and comparing these values to those of the initial saline water. Infrared (IR) imaging was employed to investigate the heat localization properties of the photoabsorber and its influence on the evaporation rate of the synthesized samples.

2.11 Structural analysis

Figure 4 presents characterization data for the starting materials used in the nanocomposite synthesis. Specifically, Fig. 4a displays the X-ray diffraction (XRD) patterns of pure graphite and synthesized graphene oxide (GO), while Fig. 4b shows the absorption spectrum of the synthesized GO.

Figure 4a presents the XRD patterns of graphite and synthesized GO. The graphite pattern exhibits a sharp, intense peak at approximately $2\theta = 26^{\circ}$, corresponding to the (002) diffraction plane. Upon oxidation, this peak shift and broaden, appearing at approximately $2\theta = 11^{\circ}$ and corresponding to the (001) plane. This shift indicates successful oxidation of graphite to GO. Using the Scherrer equation, the calculated interlayer spacing of 8 Å for GO confirms the insertion of functional groups between the carbon layers during oxidation [53].

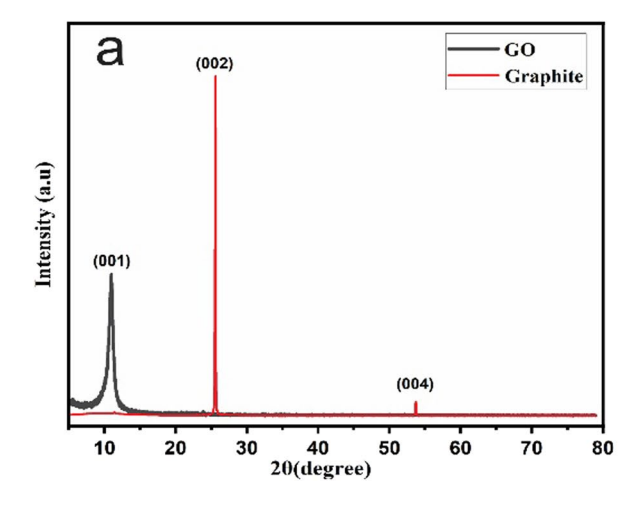
Figure 4b shows the absorbance spectrum of synthesized GO in the 200–800 nm wavelength range. Oxidized graphene exhibits a distinct peak at approximately 240 nm, corresponding to $\pi \to \pi^*$ transitions of C=C aromatic bonds. A shoulder at approximately 300 nm, assigned to $n-\pi^*$ transitions of C=O bonds, is also observed [54]. These spectral features confirm the formation of graphene oxide in the synthesis process.

Figure 5 presents X-ray diffraction (XRD) patterns of the synthesized materials. Figure 5a displays the XRD patterns of the synthesized nanoparticles (TiO_2 , $NiFe_2O_4$, ZnO, and GO), while Fig. 5b shows the XRD patterns of the synthesized GTNZ nanocomposites.

Figure 5a shows the XRD pattern of TiO₂ nanoparticles with diffraction peaks at $20 \approx 25.3^{\circ}$, 37.8°, 48.1°, 62.44°, 68.72°, 70.63°, and 74.94°. These peaks correspond to the (101), (004), (200), (105), (204), (116), (220), and (215) diffraction planes of the pure anatase phase of TiO₂ (JCPDS-No. 21–1272) [44]. Figure 5a also shows the XRD pattern of synthesized ZnO nanoparticles with diffraction peaks at $2\theta \approx 30.1^{\circ}$, 35.1° , 40.2° , 45.1° , 55.3° , 62.2° , 65° , 65.4° , 66.4° , and 70° . These peaks are attributed to the (100), (002), (101), (102), (110), (103), (112), (201), and (004) planes of the hexagonal crystal structure of the zinc oxide wurtzite phase. Also in Fig. 5a, the XRD pattern of synthesized NiFe₂O₄ shows peaks at $2\theta \approx 18.40^{\circ}$, 30.30°, 35.66°, 37.3°, 43.36°, 53.74°, 57.36°, 63.0°, 71.50°, and 74.48°. These correspond to the (111), (220), (311), (222), (400), (422), (511), (440), (620), and (533) diffraction planes of the pure spinel crystal phase, consistent with JCPDS-No. 10-0325 standard data [44].

Furthermore, the crystal sizes of the individual components (rGO, TiO2, ZnO, and NiFe2O4) were calculated using the Scherrer equation:

$$D = K\lambda/(\beta \cos\theta) \tag{7}$$



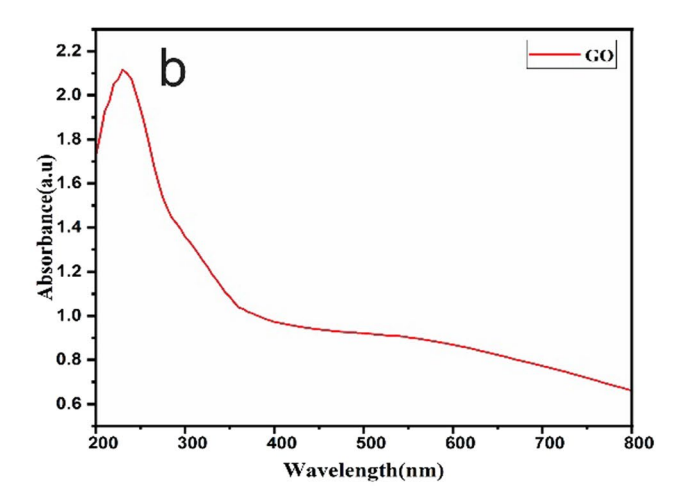
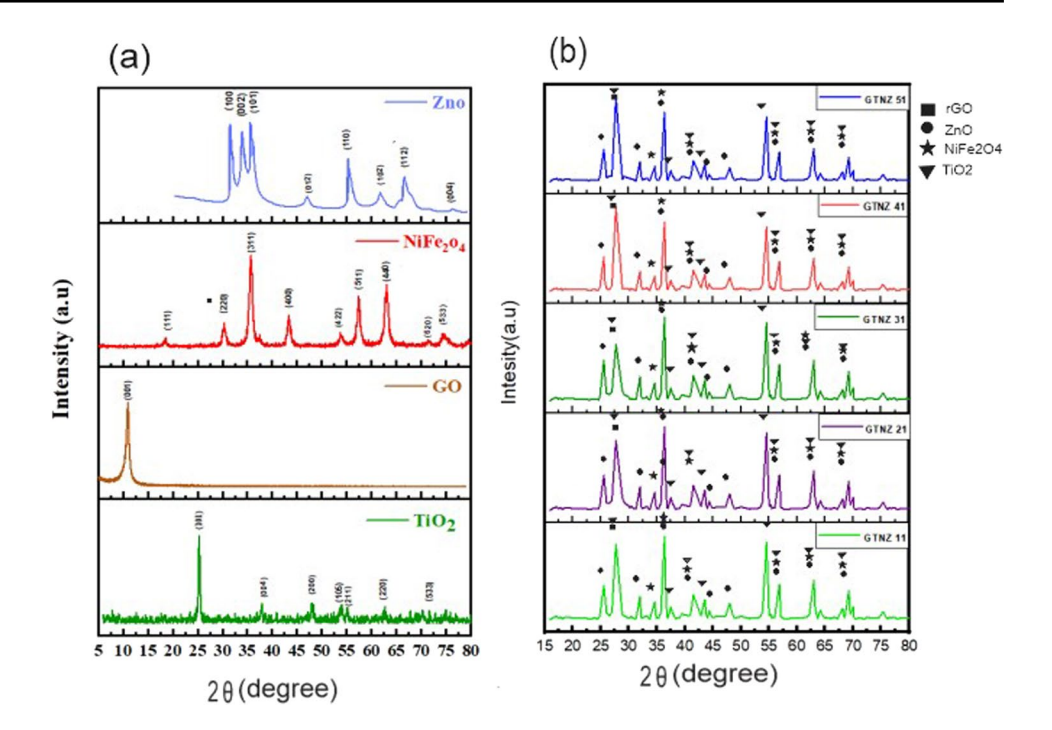


Fig. 4 a X-ray diffraction pattern of pure graphite and synthesized graphene oxide. b Absorption spectrum of the synthesized graphene oxide



Fig. 5 a X-ray diffraction pattern of the synthesized nanoparticles and **b** X-ray diffraction pattern of the synthesized GTNZ nanocomposites



where D is the crystal size, K is the Scherrer constant (0.9), λ is the X-ray wavelength (0.15418 nm), β is the full width at half maximum (FWHM) of the diffraction peak in radians, and θ is the Bragg angle.

The calculations revealed crystal sizes of 33.55 nm for GO, 16.3 nm for TiO_2 , 20.4 nm for ZnO, and 27.2 nm for $NiFe_2O_4$. These values provide insight into the nanoscale dimensions and contribute to understanding the structural properties of the synthesized materials.

Figure 5b shows the XRD pattern of photo absorber synthesized nanocomposites GTNZ 11 through GTNZ 51. The diffraction peaks for the rGO nanosheets are broad and weak, which is typical of amorphous carbon materials [55] confirmation of the partial reduction of GO to rGO in the hydrothermal process. Although the XRD spectra of all samples exhibit similar overall patterns, quantitative variations in peak intensities and widths are observed. Specifically, a noticeable reduction in the intensity of the diffraction peak corresponding to the TiO_2 anatase (101) plane, located at $2\theta = 25-30^\circ$, is observed. This reduction in intensity is attributed to the increasing presence of rGO sheets within the nanocomposite, which can interfere with the crystalline growth of TiO_2 . Furthermore, the strong diffraction peak of TiO_2 anatase at approximately 25° overlaps with and obscures the characteristic broad (002) peak of rGO. This overlap, coupled with the relatively low intensity of the rGO peak, results in the rGO peak being indistinguishable in the nanocomposite XRD spectra [56, 57].

Figure 6a, b present FESEM images of the synthesized GTNZ 11 to GTNZ 51 nanocomposites at 200 nm and 1 μ m scale bars, respectively. Figure 6a reveals a uniform distribution of TiO₂, NiFe₂O₄, and ZnO nanoparticles. These nanoparticles demonstrate a predominantly spherical morphology with an average size of approximately 25–30 nm. The rGO nanosheets exhibit a layered structure with lateral dimensions ranging from hundreds of nanometers to several micrometers.

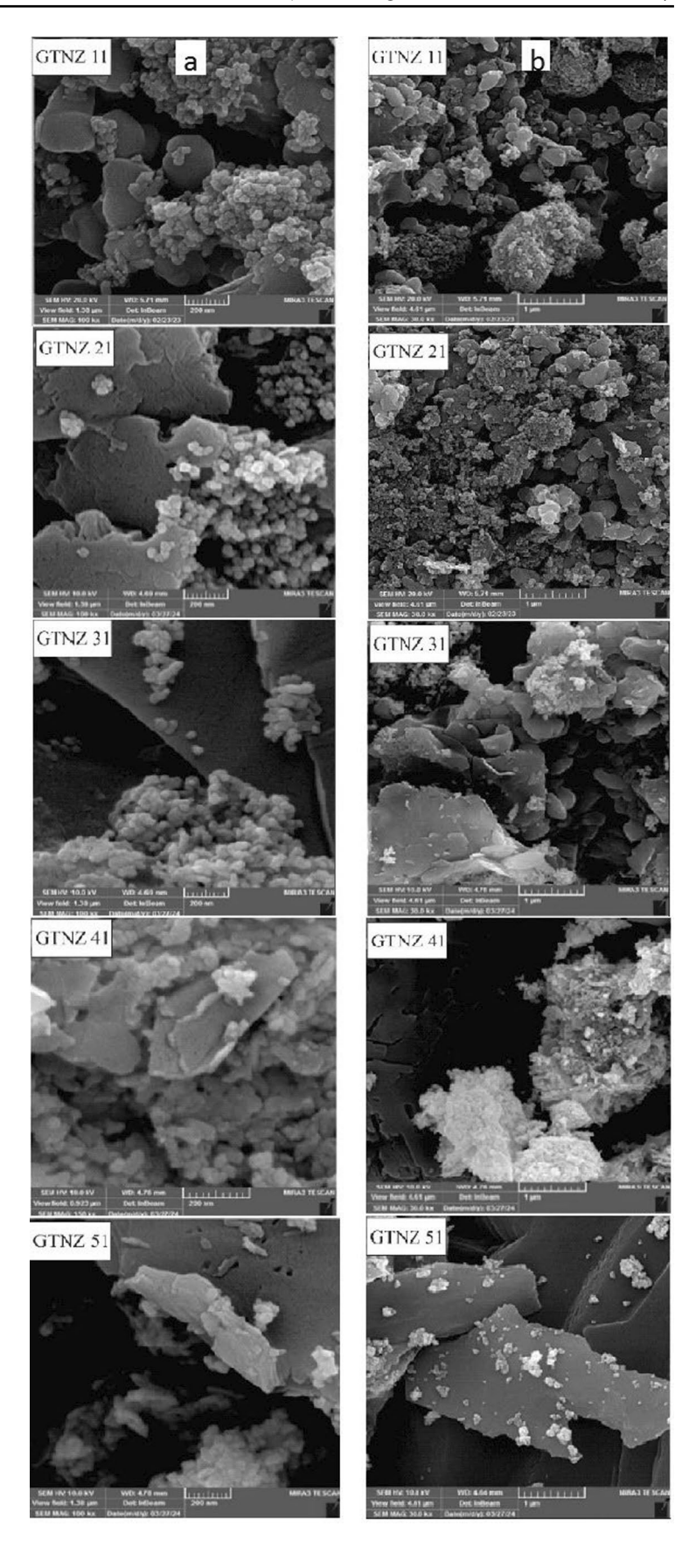
The FESEM images indicate that increasing the rGO content within the nanocomposites leads to a noticeable decrease in nanoparticle density and a reduction in nanoparticle agglomeration. This observation aligns with the synthesis conditions and the increasing rGO mass ratio from 1:1 to 5:1 relative to the other nanoparticles. In GTNZ 11, the rGO nanosheets are largely covered by TiO_2 , TiC_2O_4 , and TiC_3O_4 and TiC_3O_4 and TiC_3O_4 and TiC_3O_4 and TiC_3O_4 are exposed rGO planes devoid of nanoparticles.

Across all samples, the TiO_2 , $NiFe_2O_4$, and ZnO nanoparticles are uniformly dispersed, with no evidence of specific nanoparticle agglomeration. This homogeneous distribution is evident in the FESEM images, characterized by the consistent dispersion of nanoparticles with distinct color contrasts.

To confirm the presence and relative abundance of constituent elements within the nanocomposites, Energy-Dispersive X-ray spectroscopy (EDX) analysis was performed. The resulting spectra are presented in Fig. 7. Due to the observed uniform nanoparticle distribution in the Field-Emission Scanning Electron Microscopy (FESEM) images and the significant



Fig. 6 Field emission scanning electron microscopy (FESEM) images of synthesized nanocomposite at **a** 200 nm and **b** 1 μm scale bar





(2025) 5:83

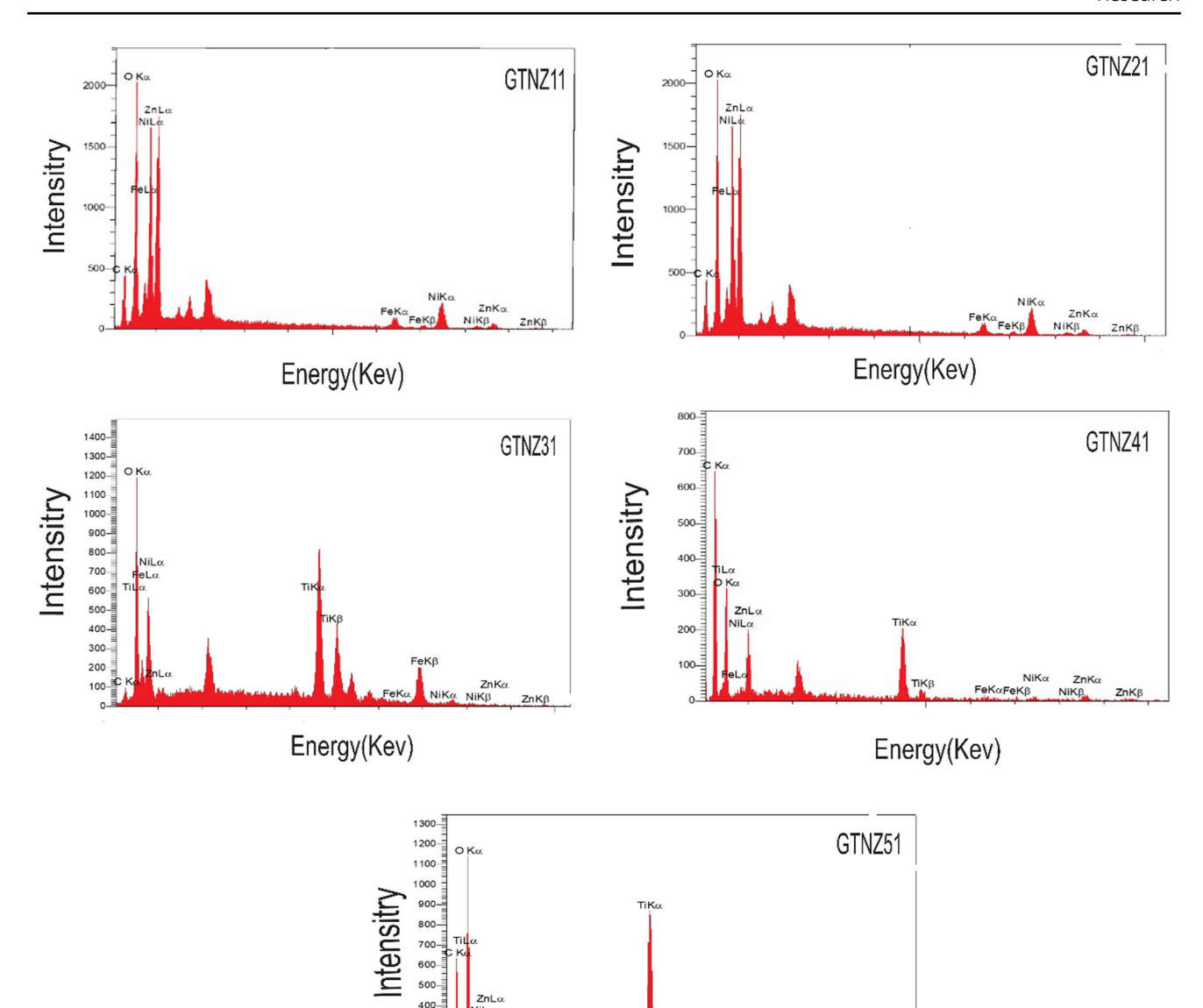


Fig. 7 EDX analysis of the synthesized nanocomposites GTNZ 11 trough GTNZ 51

300 200

size difference between the nanoparticles and the reduced graphene oxide (rGO) nanosheets, EDX spectra were acquired from multiple, randomly selected points across each nanocomposite sample. This provided a representative average elemental composition.

Energy(Kev)

As depicted in the EDX spectra, a progressive increase in the carbon (C) signal is evident from GTNZ 11 to GTNZ 51. This trend correlates with the increasing initial weight ratio of graphene oxide (GO) used in the nanocomposite synthesis, reflecting the expected increase in rGO content. Furthermore, the elemental analysis summarized in Table 2 validates the presence of all expected elements within the nanocomposites.

To further investigate the surface characteristics and porosity of the GTNZ41 nanocomposite, Brunauer–Emmett–Teller (BET) and Barrett-Joyner-Halenda (BJH) analyses were performed. These analyses provide valuable insights into the specific surface area, pore size distribution, and pore morphology, which are critical factors influencing the material's performance in various applications, including catalysis and adsorption. The nitrogen adsorption–desorption isotherm and BJH pore size distribution are presented in Fig. 8a, b, respectively.



Table 2 Elemental analysis of the synthesized nanocomposites

Sample	Sample Elemental analysis	alysis										
	U		0		i=		Z		Fe		Zn	
	Weight per- centage (%)	Veight per- Atomic per- entage (%) centage (%)		Weight per-Atomic per- centage (%) centage (%)	Weight per- centage (%)	Veight per- Atomic per- entage (%) centage (%)	Weight per- Atomic per- centage (%) centage (%)	Atomic per- centage (%)	Weight per- Atomic per- centage (%) centage (%)	Veight per- Atomic per- entage (%) centage (%)	Weight per- Atomic centage (%) percent:	per- Atomic (%) percentage (%)
GNTZ11 15.90	15.90	36.2	49.9	50.5	13.52	5.9	2.2	1.5	3.8	0.5	14.5	5.1
GNTZ21	24.9	35.5	50.55	55	12.62	4.1	2.1	1	2.5	0.3	6.9	4
GNTZ31	28.1	33.1	50.3	58.1	12.1	4.01	2	9.0	2.01	0.2	5.4	3.5
GNTZ41	47.88	60.93	35.88	34.28	11.26	3.59	6.0	0.2	0.44	0.12	3.62	9.0
GNTZ51	53.1	63.01	38.12	30.5	7.8	2.1	0.5	0.1	0.21	60.0	2.1	4



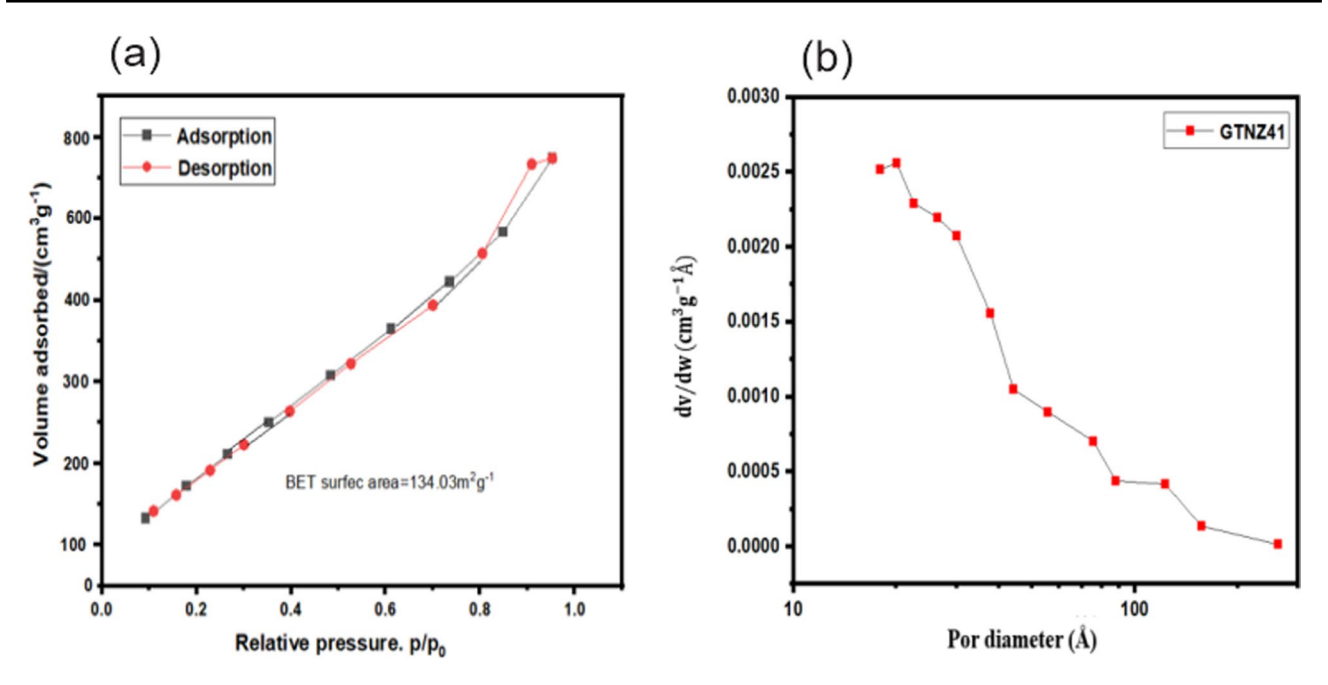


Fig. 8 a Nitrogen adsorption—desorption isotherm of the GTNZ41 nanocomposite, exhibiting a Type IV isotherm characteristic of mesoporous materials. b Barrett-Joyner-Halenda (BJH) pore size distribution of the GTNZ41 nanocomposite

The nitrogen adsorption—desorption isotherm of the GTNZ41 nanocomposite exhibits a Type IV isotherm, characteristic of mesoporous materials. This isotherm is characterized by a gradual increase in adsorption at low pressures, followed by a more pronounced increase at higher pressures due to capillary condensation in mesopores. The presence of a hysteresis loop, likely of type H3 or H4, suggests the presence of slit-shaped pores or narrow mesopores, indicative of layered structures or specific pore geometries. These features highlight the mesoporous nature and surface characteristics of the GTNZ41 material. Specifically, the material exhibits a wide distribution of pore sizes, which can be advantageous for various applications such as gas storage, adsorption of specific materials, and catalytic processes. Materials with smaller pores possess a higher specific surface area, which is crucial for adsorption and chemical reactions.

The Barrett-Joyner-Halenda (BJH) pore size distribution analysis of the GTNZ41 nanocomposite further supports the mesoporous nature of the material, consistent with the Type IV isotherm observed in the BET analysis. The BJH analysis reveals a broad pore size distribution, confirming the presence of pores with a wide range of sizes. This characteristic is beneficial for applications requiring efficient mass transport and high surface area, such as catalysis and adsorption. The presence of a hysteresis loop, similar to the BET isotherm, suggests the existence of specific pore shapes, such as slit-shaped or cylindrical pores, which contribute to the material's unique surface properties [50, 58].

While this study provides a thorough analysis of the nanocomposite, future research should include X-ray Photoelectron Spectroscopy (XPS). XPS would offer valuable insights into surface chemistry, including chemical composition, oxidation states, bonding, and functional groups. This analysis would enhance understanding of the material's properties and aid in optimizing its performance for various applications.

2.12 Photocatalytic properties

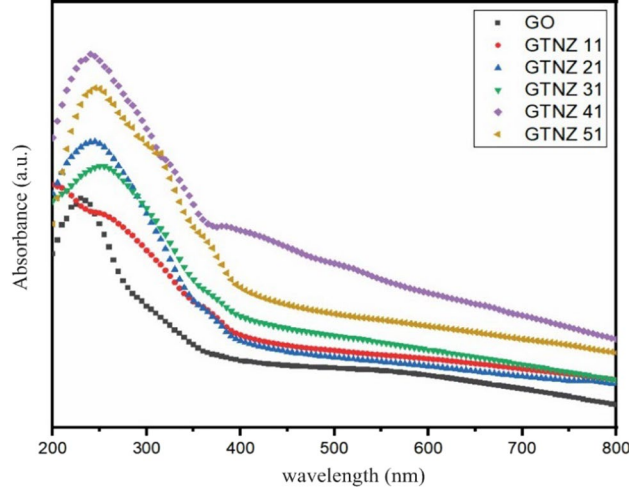
In order to investigate the photocatalytic properties of synthesized nanocomposites, the absorbance spectrum of the samples was recorded in the 200–800 nm range. Figure 9 shows that sample GTNZ 41 has the most absorption in the UV, visible and near IR region. Since most of the light reaching earth from sun (97%), are in the visible and IR spectrum [59], sample GTNZ 41 has the most potential for absorbing the sun light and used in DSSG application.

Figure 10 illustrates the photocatalytic degradation of methylene blue. Figure 10a presents the concentration of methylene blue as a function of UV light irradiation time for different nanocomposites. Figure 10b shows the absorption spectrum of sample GTNZ 41 in the methylene blue solution as a function of UV light illumination time.

Figure 10a illustrates the corresponding relative MB concentration changes versus UV light exposure time. This figure reveals, the best photocatalytic activity is related to sample GTNZ 41 which more efficiently destroys MB under UV



Fig. 9 Absorption spectrum of the synthesized nanocomposites in the 200–800 nm wavelength



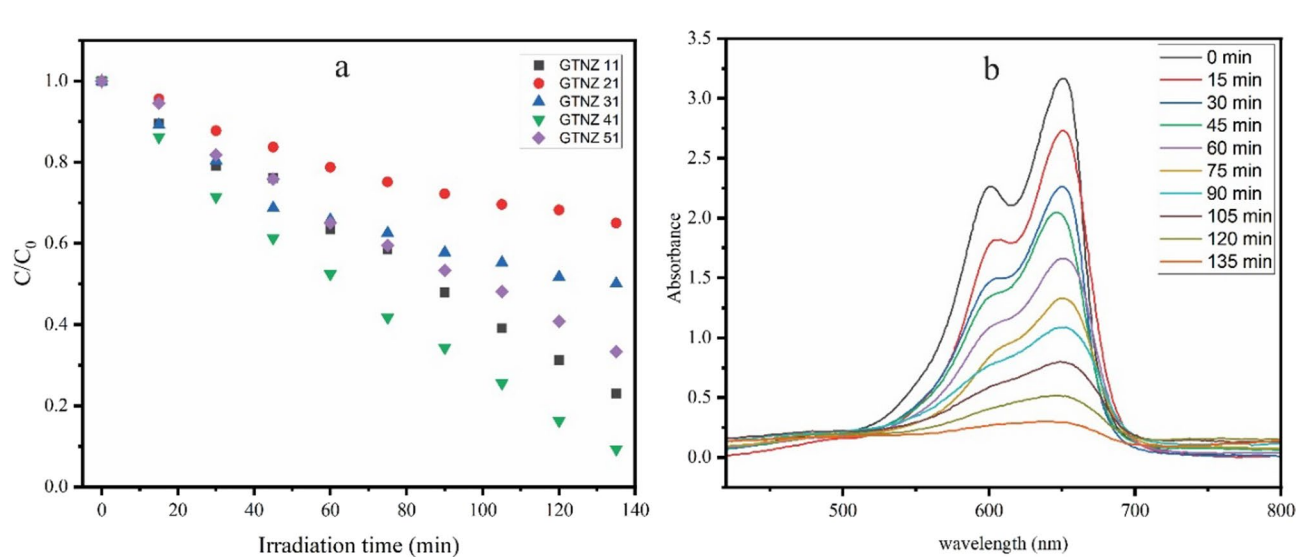


Fig. 10 a Methylene blue concentration as a function of UV light irradiation time for different nanocomposites and **b** absorption spectrum of sample GTNZ 41 in methylene blue solution as a function of UV light illumination time

illumination. The reason why the sample GTNZ 51, which had good absorbance in the UV region does not show better UV photocatalytic can be attributed to other factors like electron–hole recombination rate which is important in photocatalytic properties. Figure 10b shows the absorption spectrum of sample GTNZ 41 in MB solution for different UV light exposure time.

According to what we understood from the optical properties of the prepared nanocomposites, the most promising candidate for using in a DSSG system as a photocatalytic and photoabsorber material and producing drinking water from sea water is GTNZ 41 which have the most absorbance of light in the sun spectrum and is most efficient in destroying MB dye which can be used in sanitizing waste water application.

To assess the individual contributions of the nanocomposite components, photocatalytic degradation tests of methylene blue (MB) were conducted using ZnO, TiO_2 , TiO_2 , TiO_2 , TiO_3 , TiO_4 , and GO separately under identical condition with nanocomposite MB degradation test. Figure 11 shows the MB degradation of the GO, TiO_2 , TiO_3 , TiO_4 nanostructures. Notably, TiO_4 and TiO_4 nanocomposite higher MB degradation efficiencies compared to the GTNZ 41 nanocomposite. This suggests that these individual oxides possess inherent photocatalytic activity that may surpass the composite under these specific degradation conditions.

However, it is crucial to consider the broader context of our research, which focuses on the application of the GTNZ nanocomposite for solar steam generation (DSSG). Despite strong photocatalytic abilities, TiO₂ and ZnO lack



(2025) 5:83

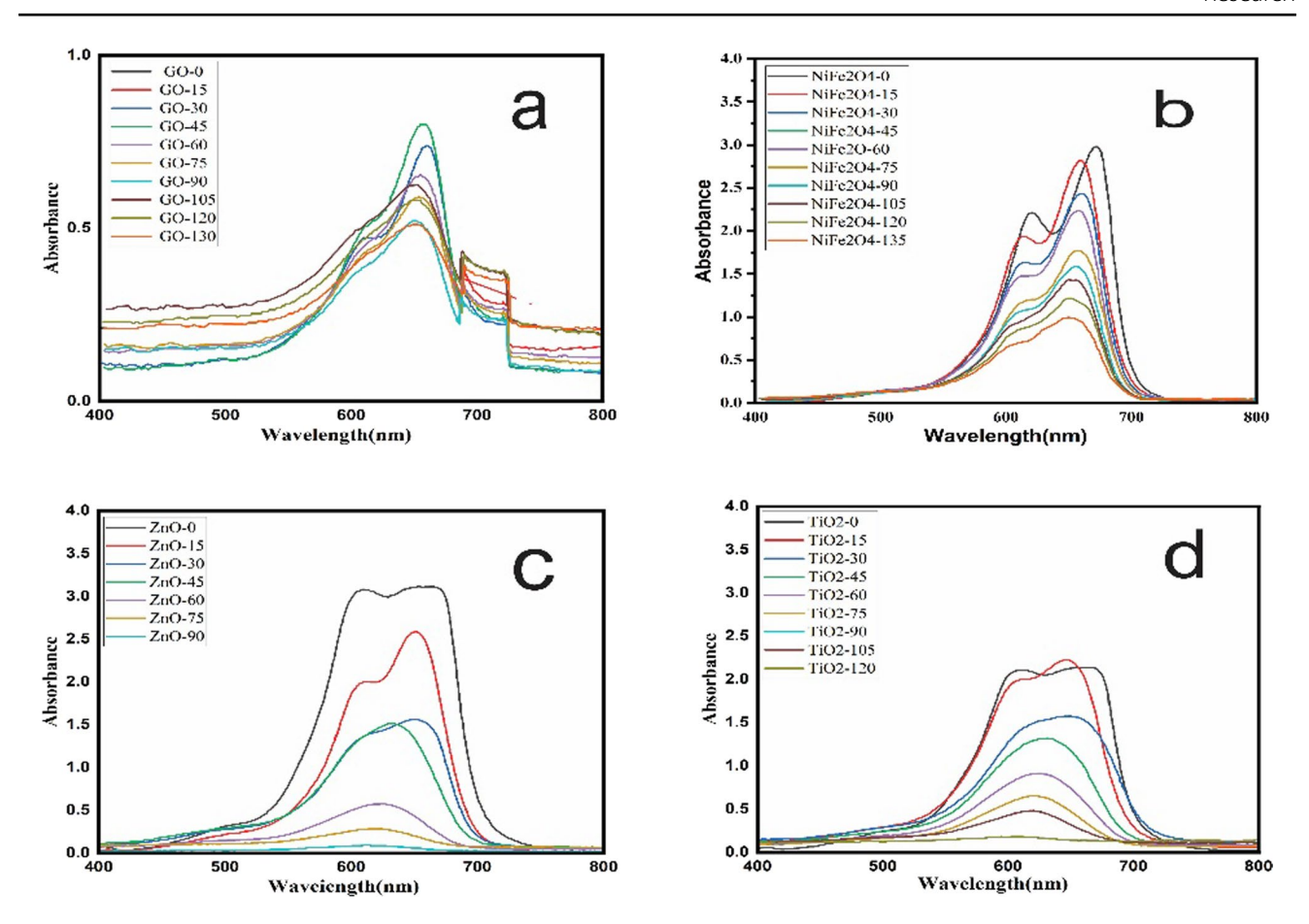


Fig. 11 Photocatalytic degradation of methylene blue (MB) under UV light for individual nanostructures, **a** GO, **b** NiFe₂O₄ **c** ZnO and **d** TiO₂

the essential combined photothermal and structural properties needed for efficient DSSG application. The GTNZ nanocomposite, by contrast, demonstrates:

Enhanced photothermal conversion: The presence of rGO in the GTNZ nanocomposite facilitates efficient light-to-heat conversion and heat localization at the evaporation surface, crucial for DSSG.

Synergistic effects: The heterojunctions formed among the components, including ${\rm TiO_2}$ and ${\rm ZnO}$, contribute to efficient charge separation, potentially enhancing long-term photocatalytic stability and water purification during DSSG. Broad spectrum absorption: The combination of the components and especially the rGO allow for a broad spectrum light absorption.

Therefore, while the individual photocatalytic tests reveal the superior degradation potential of ${\rm TiO_2}$ and ZnO in this isolated context, the GTNZ nanocomposite's combined photothermal, structural, and synergistic properties make it a more promising candidate for integrated DSSG and water purification applications. The nanocomposite is designed for a system that uses the heat to create clean water, and also uses the photocatalytic properties to remove organic pollutants.

To further understand the electronic properties of the synthesized materials, Tauc plots were generated from the UV–Vis absorption spectra to determine the band gap energies. Figure 12 presents the Tauc plots for the individual nanoparticles (GO, TiO₂, NiFe₂O₄, and ZnO) and the GTNZ 41 nanocomposite using Eq. 4.

By extrapolating the linear portion of the $(\alpha hv)^{1/2}$ vs. hv plot to the hv axis, the band gap energies were determined. The individual nanoparticles exhibited band gap energies of 1.5 eV for GO, 3.11 eV for TiO₂, 2.0 eV for NiFe₂O₄, and 3.1 eV for ZnO. Notably, the GTNZ 41 nanocomposite displayed a band gap energy of 1.40 eV.

The observed reduction in the band gap of the GTNZ 41 nanocomposite compared to the individual nanoparticles suggests a synergistic effect arising from the heterojunction formation and the presence of rGO. This reduction can enhance the absorption of visible light, which is crucial for improved photocatalytic activity. The lower band gap of GTNZ 41, along with the heterojunctions, facilitates efficient charge separation and transfer, contributing to its superior photocatalytic performance compared to the other nanocomposites (GTNZ 11–GTNZ 51) as previously discussed



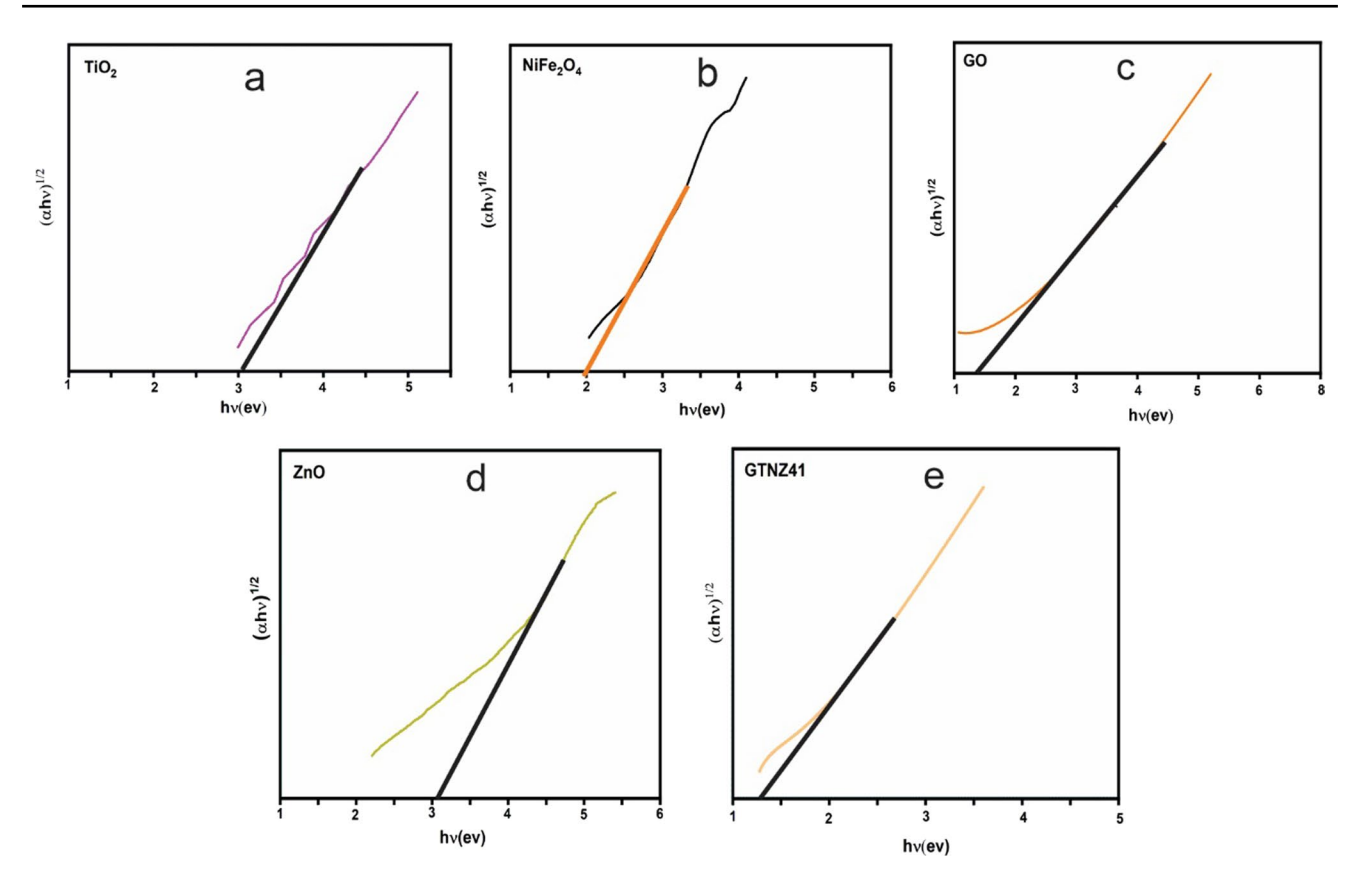


Fig. 12 Tauc plots for a TiO₂, b NiFe₂O₄, c rGO, d ZnO nanoparticles, and e GTNZ 41 nanocomposite

in this section. This band gap reduction is consistent with the enhanced methylene blue degradation observed for GTNZ 41, indicating that the nanocomposite can utilize a broader spectrum of solar light for photocatalytic processes.

To gain further insight into the electronic band structure of the synthesized materials, the valence band (VB) and conduction band (CB) positions were estimated using the Butler-Ginley equations (Eqs. 5 and 6).

The absolute electronegativity (χ) of the GTNZ 41 nanocomposite was estimated as the weighted average of the electronegativities of its constituent materials (TiO₂, NiFe₂O₄, ZnO, and rGO), considering the respective weight ratio of the ingredients in the composite.

$$\chi_{GTNZ41} = \frac{(4 \times \chi_{rGO}) + \chi_{ZnO} + \chi_{TiO2} + \chi_{Nife2O4}}{4 + 1 + 1 + 1} \tag{8}$$

where E_{VB} and E_{CB} are the valence and conduction band edge potentials, respectively, χ is the absolute electronegativity of the semiconductor, Ee is the energy of free electrons on the hydrogen scale (approximately 4.5 eV), and E_q is the band gap energy determined from the Tauc plots (Fig. 12).

Figure 13 illustrates the estimated VB and CB positions for the individual nanoparticles (GO, TiO2, NiFe2O4, and ZnO) and the GTNZ 41 nanocomposite. The calculations revealed that the VB positions were 0.95 eV, 2.86 eV, 1.45 eV, 1.74 eV and -0.92 eV, while the CB positions were -0.55, -0.24 eV, -1.65 eV, -0.26 eV and -2.32 eV, for GO, TiO₂, ZnO, NiFe₂O₄ and GTNZ 41 respectively.

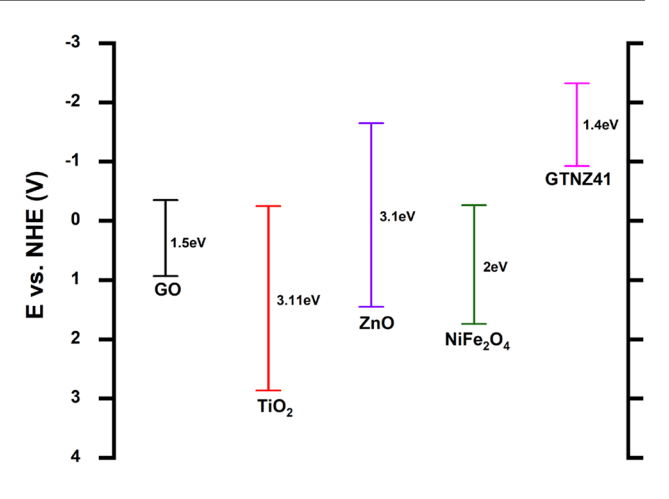
The calculated band edge positions provide valuable information regarding the charge transfer properties and photocatalytic activity of the materials. The specific alignment of the VB and CB positions in the GTNZ 41 nanocomposite suggests a favorable heterojunction formation, which can facilitate efficient charge separation and enhance photocatalytic performance.

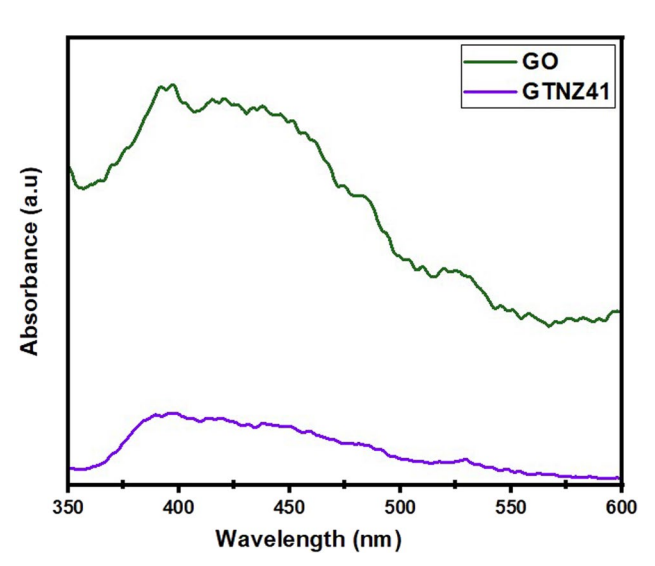
To further investigate the optical properties of the GO and GTNZ41 nanocomposite, photoluminescence (PL) spectroscopy was performed, and the resulting spectra are presented in Fig. 14.



Fig. 13 Schematic illustration of the calculated valence band (VB) and conduction band (CB) positions for GO, TiO₂, NiFe₂O₄, ZnO nanoparticles, and GTNZ 41 nanocomposite

Fig. 14 Photoluminescence (PL) spectra of graphene oxide (GO) and the GTNZ41 nanocomposite





By analyzing Fig. 14, key differences in the photoluminescence (PL) spectra of graphene oxide (GO) and the GTNZ41 nanocomposite can be observed. In the GO sample, the main peak is located at a wavelength of approximately 370–380 nm. In the GTNZ41 sample, the main peak is shifted to a wavelength of approximately 390–400 nm.

This red-shift (shift to higher wavelengths) of the PL peak in GTNZ41 indicates a modification in the electronic structure of the nanocomposite. This change can be attributed to several factors, including:

Increased nanoparticle size: Larger nanoparticles can lead to changes in the band structure and thus the emission wavelength.

Alterations in the energy band structure: The formation of the nanocomposite can alter the energy band structure due to interactions between the components.

Reduction of surface defects: The combination of nanoparticles may lead to a decrease in surface defects, which can affect the emission properties.

Furthermore, the PL intensity of the GTNZ41 sample is higher than that of the GO sample. This increase in intensity suggests a higher radiative recombination rate in GTNZ41 compared to GO. The reasons for the enhanced PL intensity in GTNZ41 can be attributed to:

Reduced non-radiative recombination: The nanocomposite formation likely reduces non-radiative recombination pathways. Surface defects often act as centers for non-radiative recombination, and such defects reduction leads to increased radiative emission.

Improved luminescence properties: The combination of nanoparticles in GTNZ41 may modify the energy levels, increasing the probability of electronic transitions and thus enhancing the emission intensity.

Influence of internal fields: The internal electric fields generated by the nanoparticles in GTNZ41 can influence electronic transitions and amplify the PL signal.



Additionally, the PL spectrum of GO exhibits a broader peak, indicating a higher density of surface defects and heterogeneity in the electronic structure. In contrast, the GTNZ41 PL spectrum is narrower and displays a more defined peak, suggesting an improvement in the crystalline structure and a reduction in surface defects [60, 61].

In conclusion, the GTNZ41 nanocomposite demonstrates superior optical performance compared to GO. The increased PL intensity and the red-shifted peak highlight the positive impact of nanoparticle integration in enhancing the luminescence properties.

2.13 Direct solar steam generation (DSSG) experiment

2.13.1 Evaporation performance of prepared photoabsorbers

Initial screening involved evaluating the absorption spectrum and photocatalytic properties of GTNZ11 to GTNZ51. Based on these preliminary tests, GTNZ41 was selected for further direct solar steam generation (DSSG) experiments. This selection was based on two key factors:

- 1. Optimal light absorption: GTNZ41 exhibited the highest absorption within the visible and infrared (IR) spectrum (97% of solar irradiance). This is crucial for efficient light-to-heat conversion.
- 2. Superior photocatalytic activity: GTNZ41 demonstrated the most effective degradation of methylene blue (MB) under UV light exposure, indicating strong photocatalytic properties.

Prepared photoabsorbers suspensions with different GTNZ 41 nanocomposite concentration, were drop-cast on poplar wood substrate. Five photoabsorber samples were prepared with varying concentrations of GTNZ41 (1.5, 3, 4.5, 6 and 7.5 g L^{-1}). These samples were designated as S1–S5.

Figure 15 presents the direct solar steam generation (DSSG) performance of the synthesized nanocomposites under 3 sun illumination. Specifically, Fig. 15a shows the mass reduction per unit area, Fig. 15b displays the evaporation rate, Fig. 15c illustrates the evaporation efficiency, and Fig. 15d presents the top sensor temperature changes for different samples.

To optimize nanocomposite concentration for direct solar steam generation (DSSG), we evaluated the evaporation performance of samples S1 through S5 using a custom-built DSSG system. Figure 15a illustrates the mass reduction per unit area for each photoabsorber sample, alongside seawater and bare wood, under 3 sun illumination over 40 min.

Evaporation performance was quantified by measuring the mass of evaporated seawater. A greater reduction in seawater mass directly correlates with enhanced vapor production and, therefore, improved DSSG performance.

As evidenced in Fig. 15a, seawater alone exhibited the lowest mass reduction, registering 0.329 kg/m². Conversely, sample S4, with a nanocomposite concentration of 6 g/L, demonstrated the highest mass reduction, attaining 2.71 kg/m². This result decisively indicates S4's superior vapor generation capacity.

The vertical axis of Fig. 15a presents the mass reduction per unit area (Δm) of the photoabsorber, expressed in kg/m². This data is plotted as a function of time, showcasing the progression of mass reduction throughout the 40-min DSSG experiment under 3 sun illumination. For more clarification this relation is as follow:

$$\Delta m = \frac{m_t - m_0}{A} \tag{9}$$

Which in this relation m_t is the mass of seawater of the beaker at any time of the DSSG experiment, m_0 is the seawater of the beaker at the beginning of the DSSG experiment and A is the surface area of the photoabsorber.

In bare wood, micro channels supply water at the surface and reduce the heat loss to the bulk water and hence the interfacial evaporation increases as much as 0.164 kg m^{-2} in comparison with seawater. All the samples show better evaporation ability than seawater and bare wood which implies nanocomposite is successful in absorbing light and generating heat for evaporating water. In samples S1-S4, with increasing concentration, evaporation increases but by increasing nanocomposite concentration from 6 to 7.5 g L^{-1} , evaporation decreases which can be attributed to increased light scattering and reduction in light absorbance at the water-photoabsorber interface. The mass reduction through interfacial vapor generation in DSSG experiment is about 0.329, 0.493, 0.645, 1.55, 1.60, 2.71 and 1.89 kg m^{-2} for seawater, bare poplar wood, S1, S2, S3, S4 and S5 respectively.



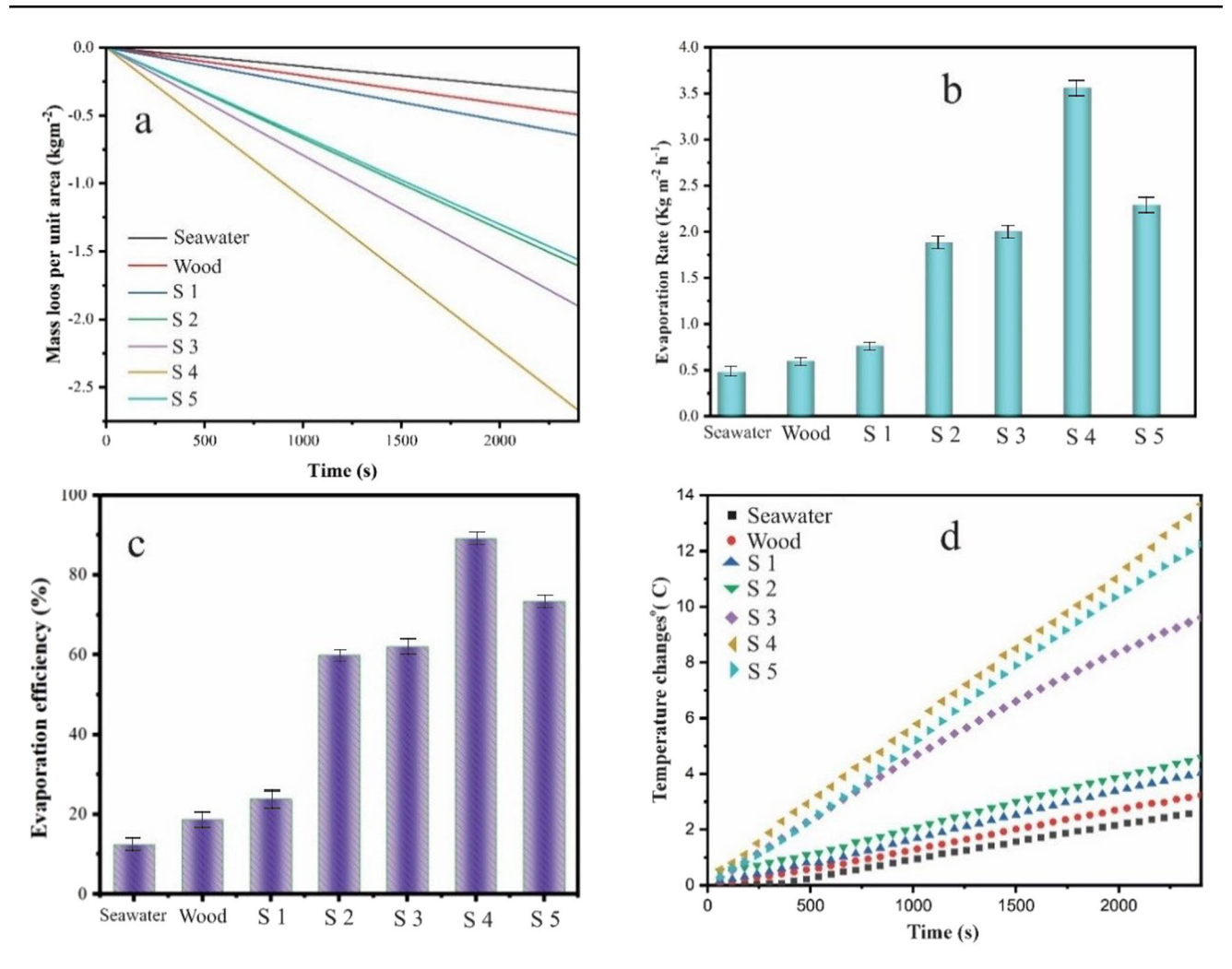


Fig. 15 a Mass reduction per unit area **b** evaporation rate **c** evaporation efficiency and **d** top sensor changes for different samples under 3 sun illumination

Better performance in mass reduction through interfacial vapor generation in sample S4 in comparison with bare wood, S1, S2 and S3 is related to the nanocomposite concentration on the photoabsorber. This result show that with increasing the concentration of nanocomposite, it increases the heat generation through solar radiation absorption which causes more vapor generation and increases the mass reduction. By increasing the nanocomposite concentration to 7.5 g L⁻¹, water mass reduction decreases which can be due to the reduced micro channels performance as a result of increased nanocomposite concentration and hence reduced water supply at the water–air interface and/or increased light scattering and reduced heat generation at the interface. In order to better understand the mass reduction efficiency of the prepared samples, evaporation rate of different samples was calculated using Eq. (1) and compared with seawater and bare poplar wood. Figure 15b shows the evaporation rate for seawater, bare wood, and samples S1 through S5.

The evaporation rate, defined as the mass reduction per unit area per unit time, was calculated using Eq. (1) and is presented in Fig. 15b. The data reveal a clear trend correlating with the nanocomposite concentration, mirroring the trend in mass loss per unit area observed in Fig. 15a.

Specifically, seawater exhibited the lowest evaporation rate (0.49 kg m $^{-2}$ h $^{-1}$), and bare poplar wood in seawater showed a slightly higher rate (0.59 kg m $^{-2}$ h $^{-1}$). The evaporation rate progressively increased with increasing nanocomposite concentration from samples S1 to S4 (0.81, 1.88, 2.10, and 3.53 kg m $^{-2}$ h $^{-1}$, respectively). This increase indicates enhanced photothermal conversion and subsequent water vaporization due to the increased light absorption of the nanocomposite.

However, a notable decrease in evaporation rate was observed for sample S5 (2.22 kg m⁻² h⁻¹) compared to S4 (3.53 kg m⁻² h⁻¹). This reduction, despite a further increase in nanocomposite concentration from 6 g L⁻¹ (S4) to 7.5 g L⁻¹ (S5),



aligns with the observed decrease in mass loss per unit area for S5 (Fig. 15a). This suggests that beyond optimal concentration, the nanocomposite may experience aggregation or other phenomena that hinder its light-to-heat conversion capabilities.

To ensure the reliability and reproducibility of the evaporation rate measurements, each experiment was conducted in triplicate. Error bars, representing the standard deviation of these three independent measurements, are included in Fig. 15b. This approach allows for the quantification of uncertainties inherent in the experimental setup and provides a measure of data variability.

Several potential sources of error could have influenced the evaporation rate measurements. Firstly, fluctuations in ambient temperature and humidity, despite attempts to maintain consistent laboratory conditions, may have introduced variability in the evaporation process. To minimize heat loss to the surroundings and ensure accurate temperature monitoring, the beakers containing seawater samples were insulated thermally and equipped with calibrated temperature sensors. Secondly, minor variations in solar irradiance, even with the use of a controlled light source, could have affected the photothermal conversion and subsequent evaporation rates. Thirdly, the precision of the electronic balance used to measure mass loss is inherently limited, introducing a small degree of uncertainty in the recorded data.

The standard deviation provides a statistical measure of the dispersion of the data around the mean. The relatively small standard deviations observed in Fig. 15b indicate a high degree of reproducibility in the evaporation rate measurements, suggesting that the experimental setup was robust and the influence of the aforementioned errors was minimized. The calculated evaporation rates along with the corresponding standard deviations (SD), are presented in Table 3.

The evaporation efficiency of seawater, bare poplar wood in seawater, and poplar wood coated with varying concentrations of the photoabsorber (samples S1–S5) was calculated using Eq. (3) and is presented in Fig. 15c. As anticipated, the trend in evaporation efficiency closely mirrors that observed for the evaporation rate (Fig. 15b).

Seawater alone exhibited the lowest evaporation efficiency, approximately 12.37. The presence of bare poplar wood in seawater increased the efficiency to 18.62. Notably, all samples coated with the photoabsorber demonstrated significantly higher evaporation efficiencies compared to seawater and seawater with bare wood.

Increasing the photoabsorber concentration from 1.5 g L^{-1} (sample S1) to 6 g L^{-1} (sample S4) resulted in a progressive increase in evaporation efficiency, reaching approximately 88.89. This aligns with the corresponding increase in evaporation rate, indicating enhanced photothermal conversion. However, a decrease in evaporation efficiency to 73.23 was observed for sample S5 (7.5 g L^{-1}), consistent with the reduced evaporation rate.

The standard deviations which were calculated from triplicate experiments, are represented by error bars in Fig. 15c where it reflects the variability in evaporation efficiency under the experimental conditions.

The calculated evaporation efficiencies along with the corresponding standard deviations (SD) for different samples are presented in Table 3. This table provides a comprehensive summary of the experimental results, allowing for a direct comparison of the performance of different samples. The values presented in Table 3 correspond to the data graphically represented in Fig. 15b, c, providing a numerical complement to the visual representation of the results.

2.13.2 Light-to-heat conversion performance

In order to investigate nanocomposite light-to-heat conversion ability, top sensor temperature data were plotted as a function of time in the DSSG process. Figure 15d shows the top sensor temperature data during DSSG process for seawater, wood, and samples S1 through S5 under 3 sun irradiation. As it can be seen from this figure, seawater with no

Table 3 Evaporation rates and evaporation efficiencies for seawater, bare poplar wood in seawater, and samples S1–S5, with corresponding standard deviations (SD) calculated from triplicate measurements

Sample	Evaporation rate (kg m ⁻² h ⁻¹)	Evaporation rate SD (kg m ⁻² h ⁻¹)	Evaporation efficiency (%)	Evaporation efficiency SD (%)
Sea water	0.49	0.02	12.37	0.45
Bare wood	0.59	0.03	18.62	0.68
S1	0.81	0.05	23.89	1.13
S2	1.88	0.03	59.80	0.68
S3	2.10	0.06	61.97	1.36
S4	3.53	0.05	88.89	1.02
S5	2.22	0.08	73.23	1.81



photoabsorber has the least temperature rise as much as $2.56\,^{\circ}\text{C}$ which can be related to the heat loos trough the bulk water. Using a photoabsorber material increases the light to heat conversion ability and top sensor changes increases with increasing nanocomposite concentration from $1.5\,\text{g}\,\text{L}^{-1}$ for S1 to 6 g L⁻¹ for S4. With increasing nanocomposite from 6 to $7.5\,\text{g}\,\text{L}^{-1}$ for S5, temperature gradient decreases which is in complete agreement with our previous findings about mass loss and evaporation rate data. The most temperature increase is related to sample S4 with 6 g L⁻¹ nanocomposite concentration with more than $13.66\,^{\circ}\text{C}$. Top sensor temperature changes are 5.56, 6.23, 7.03, 7.58, 9.61, 13.66 and $12.24\,^{\circ}\text{C}$ for seawater, wood, S1, S2, S3, S4 and S5 respectively.

2.13.3 Desalination performance

For assessing solar desalination performance of the synthesized nanocomposite, conductivity, pH and salinity of sea water before and after SSG were compared. The concentration of four ions (Na⁺, K⁺, Ca²⁺ and Mg²⁺) of the seawater were measured using ICP-OES technique before and after DSSG as the salinity criterion. As Fig. 16 shows, the salinity decreases almost 4 order of magnitude with respect to the seawater. Also the salinity of the condensed water is less than that of the drinking water recommended by WHO [62] and EPA [63]. Seawater pH was 7.9 before desalination which is due to the alkaline and earth alkaline ions in the seawater. After desalination, condensed water pH reaches to 6.21 which is in complete agreement of ICP analysis revealing a dramatic decrease in ion concentration in the produced condensed water. Conductivity (κ) of the condensed water produced after desalination was measured as 2.3 μ S cm⁻¹ which is much less than that of seawater before desalination as 7500 μ S cm⁻¹ which indicates a significant decrease in the salts and ions concentration after desalination with photoabsorber S4.

2.13.4 Heat localization performance

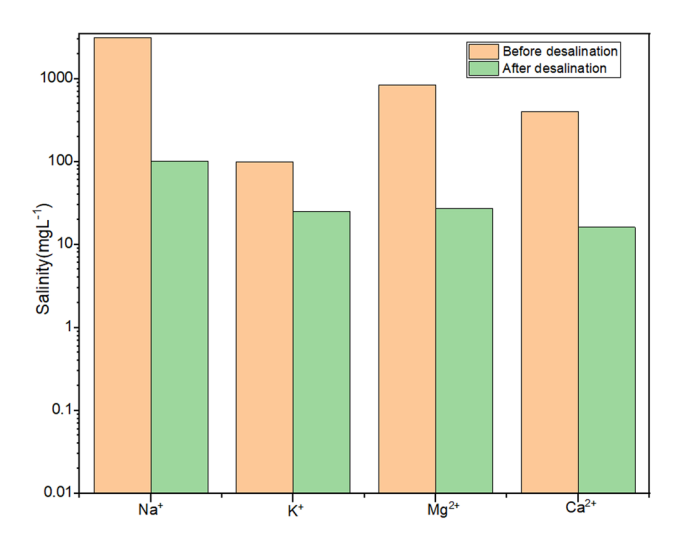
In order to better understand the photoabsorber role in a DSSG process, light-to-heat conversion behavior of the best photoabsorber (S4) was investigated using an IR camera and compared with seawater light-to-heat conversion ability.

Figure 17 presents thermal data related to the direct solar steam generation (DSSG) process. Specifically, Fig. 17a shows infrared (IR) images of seawater with and without the photoabsorber at t = 0, t = 10, and t = 40 min into the DSSG process. Figure 17b displays the temperature data recorded by the top, middle, and bottom sensors after 40 min under 3 sun illumination.

Figure 17a shows the IR pictures of seawater in the absence and presence of photoabsorber at the beginning (t = 0), 10 min and 40 min into the SSG process.

Figure 17a shows the initial and final temperature distributions in beakers containing seawater, with and without the photoabsorber. Initially, both beakers exhibited temperatures close to ambient. After 40 min, the seawater without the photoabsorber reached approximately 32 °C. In contrast, the beaker with the photoabsorber showed a surface temperature of around 40 °C, while the bottom remained significantly cooler. This temperature difference confirms that the photoabsorber confines generated heat to the evaporation surface, minimizing heat loss to the bulk water. This heat

Fig. 16 Concentration of four ions in Caspian seawater before and after desalination with GTNZ I poplar wood photoabsorber





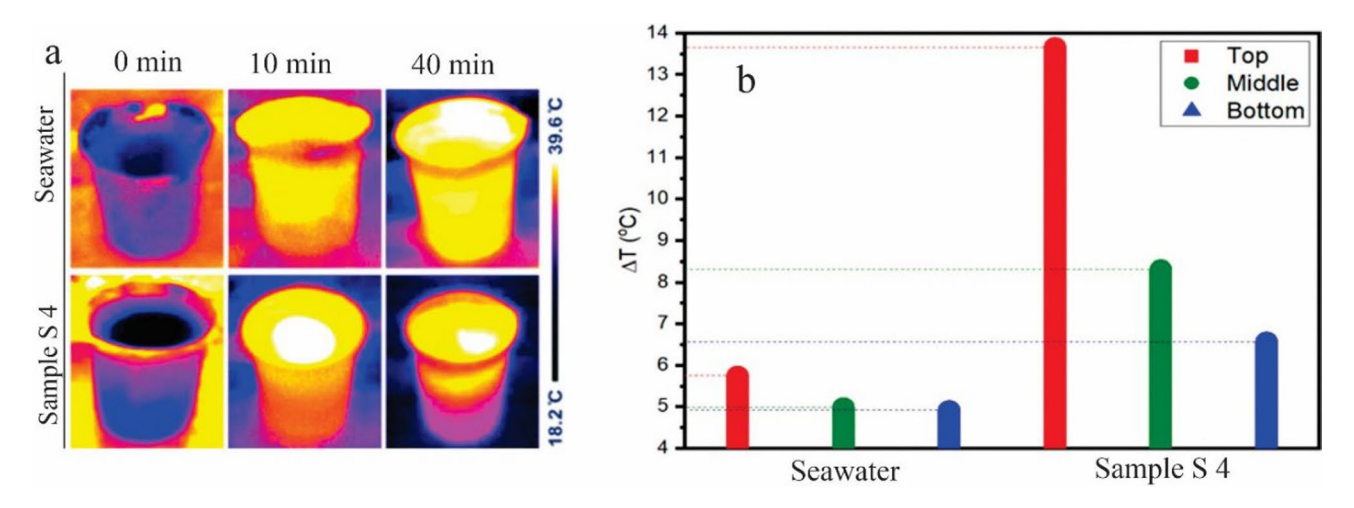


Fig. 17 **a** IR images of seawater with and without photoabsorber in t = 0, t = 10 and t = 40 min into the DSSG process. **b** Top, middle and bottom temperature sensors data after 40 min under 3 sun illumination

localization, coupled with the continuous water supply from the wood's microchannels, enhances vapor generation, making this system suitable for DSSG applications.

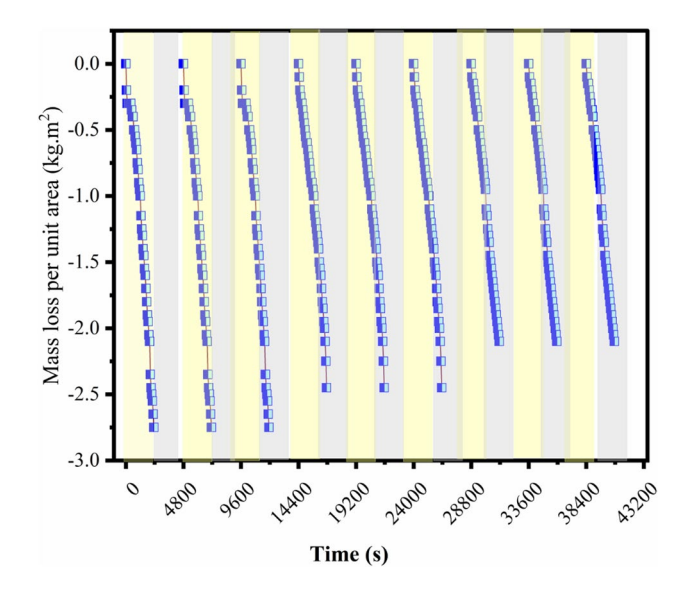
Figure 17b presents temperature data from three sensors positioned at 2, 3, and 4 cm from the beaker's bottom, with and without the photoabsorber. Without the photoabsorber, all three sensors showed a temperature rise of 5–6 °C, indicating a uniform temperature distribution. This uniformity aligns with the increased photo scattering and heat loss to the bulk water, as discussed in Sect. 3.3. In that section, we observed that seawater without a photoabsorber exhibited the lowest mass reduction. Adding bare wood increased the reduced mass per unit area, likely due to reduced heat loss.

With the photoabsorber, the sensor temperatures differed significantly: 13.66 °C, 8.12 °C, and 6.57 °C for the top, middle, and bottom sensors, respectively. These results are consistent with the heat localization observed in the IR images (Fig. 17a). The data confirms that our photoabsorber (S4) effectively absorbs sunlight, generates heat at the water/air interface, and minimizes heat loss and light scattering. This performance makes it a promising candidate for future DSSG applications.

2.13.5 Durability and cycling performance

Sustainability is an important property in evaluating the light-heat and steam generating materials for DSSG systems. Figure 18 shows the steam generation ability of sample S4 for 9 cycles of 40 min. In each cycle the beaker containing

Fig. 18 The sustainability and cycling performance of sample GTNZ 41 with 6 g L⁻¹ concentration coated on poplar wood without any treatment





(2025) 5:83

100 mL of seawater with photoabsorber was exposed to 3 sun illumination for 40 min and then the light turned off for 40 min. After 40 min of dark and replacing the container water with fresh seawater the beaker containing photoabsorber was exposed to 3 sun illumination for another 40 min without any treatment like washing the photoabsorber with DI water. As it can be seen from this figure, the photoabsorber performance does not changes and after 9 cycles without any treatment and the evaporation mass is still more than 2 kg m⁻² in 40 min. This test shows that S4 coating on poplar wood could be used as a sustainable photoabsorber in a DSSG application and keep its high efficiency for a long time.

To demonstrate the structural stability and reusability of the nanocomposite, we performed five consecutive photocatalytic degradation cycles using methylene blue (MB) as a model pollutant. Also X-ray diffraction (XRD) analysis was conducted on the nanocomposite after MB degradation.

Figure 19 illustrates the stability and recyclability of the GTNZ 41 nanocomposite. Figure 19a presents the methylene blue (MB) degradation performance of the GTNZ 41 nanocomposite over five consecutive cycles. Figure 19b shows the X-ray diffraction (XRD) pattern of the GTNZ 41 nanocomposite after MB degradation.

Figure 19a shows the photocatalytic performance of the nanocomposite over these five cycles. In the first cycle, the nanocomposite achieved a 97% degradation of MB within 135 min. After five cycles, the degradation efficiency remained high, with approximately 89% degradation of MB observed (Fig. 19a) under the same conditions mentioned in Sects. 2–6, While a slight decrease in efficiency was noted, this minor reduction suggests a potential minimal loss of active sites or surface area, rather than a significant structural change.

Figure 19b shows the XRD pattern of the nanocomposite collected after photocatalytic experiment of MB degradation. The resulting XRD patterns (Fig. 19b) show no discernible changes in the crystalline structure or phase composition compared to the initial sample (Fig. 5b). This confirms that the nanocomposite maintains its structural integrity after photocatalytic reactions.

These results unequivocally demonstrate the robust stability and excellent reusability of our rGO-TiO₂-NiFe₂O₄-ZnO nanocomposite. The consistent crystalline structure, coupled with the high retained photocatalytic activity, highlights its potential for long-term and practical applications in wastewater treatment.

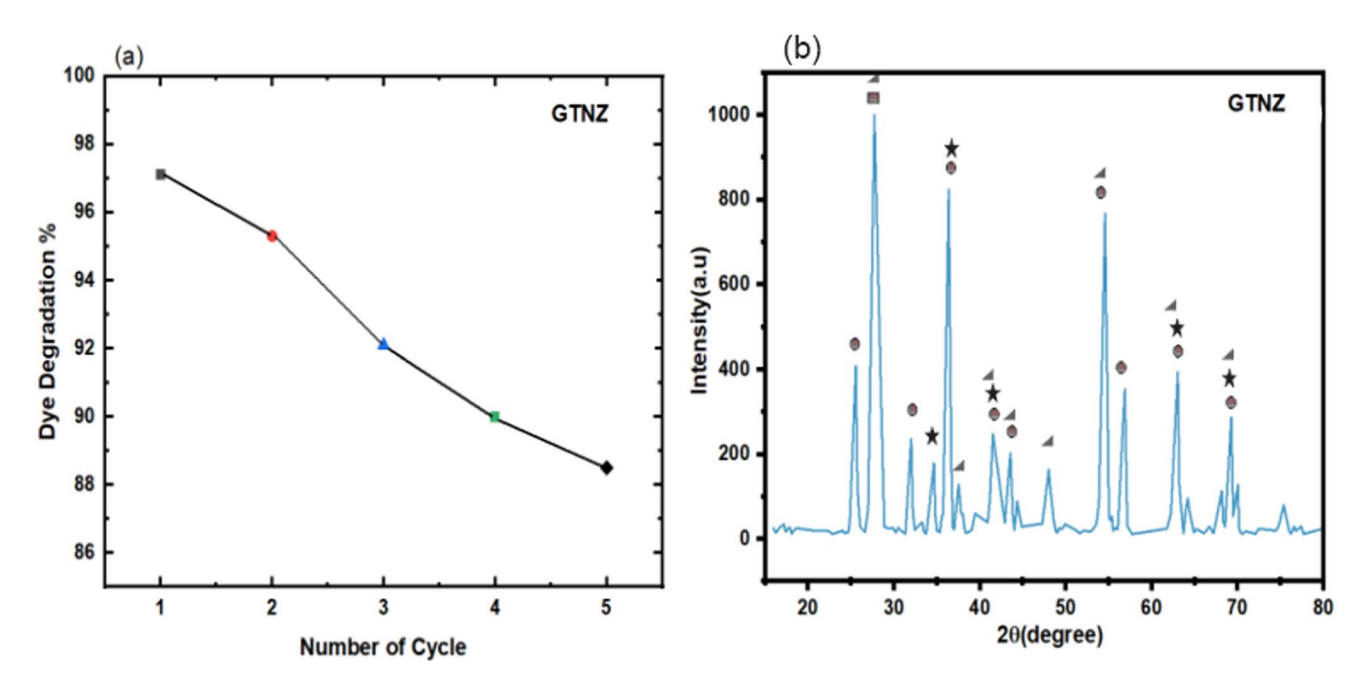


Fig. 19 a Methylene blue (MB) degradation of GTNZ 41 nanocomposite for five cycle and **b** XRD pattern of GTNZ 41 nanocomposite after MB degradation



3 Conclusion

In this research reduced graphene oxide $(rGO)/TiO_2/NiFe_2O_4/ZnO$ nanocomposites were synthesized using a simple hydrothermal method. Structural and morphological analysis shows the successful syntheses of nanocomposite with different rGO concentration in respect to other ingredients. Photocatalytic analysis revealed that nanocomposite GTNZ 41 with mass ratio of rGO:TiO₂:NiFe₂O₄:ZnO set as 4:1:1:1 has the best photocatalytic performance so this sample were choose for seawater evaporation test. For DSSG test we prepared 5 different concentrations of nanocomposite GTNZ 41 with 1.5, 3, 4.5, 6 and 7.5 g L^{-1} and coated them on poplar wood as substrate for DSSG experiment. Evaporation rate and efficiency calculation shows that sample S4 with 6 g L⁻¹ concentration shows the best evaporation performance which indicates a delicate balance between light-to-heat conversion, light scattering and heat loss can be achieved by tuning the nanocomposite concentration. IR camera images revealed the proposed photoabsorber could localize the heat at the water/air interface, prevent heat loss to the bulk water and increase the interfacial evaporation. Cycling analysis shows the stability of the photoabsorber in 9 cycle without any treatment. Good photocatalytic properties with high evaporation rate and high efficiency along with durability and sustainability make GTNZ 41 a promising candidate for DSSG application.

Acknowledgements The authors of this work appreciate the financial support of the Ferdowsi University of Mashhad Research Council, Mashhad, Iran (Grant No.3/60492).

Authors' contributions Mahmood Rezaee Roknabadi conceived of the presented idea. All authors contributed to the study conception and design. Ahmad faig Amin and Mohammad Ranjbar developed and performed the experiments. Material preparation, data collection and analysis were performed by Ahmad faiq Amin and Mohammad Ranjbar. Mahmood Rezaee Roknabadi and Mohammad behdani supervised and verified the analytical method and supervised the findings of this work. The first draft of the manuscript was written by Ahmad faig Amin and all authors commented on previous versions of the manuscript. All authors read and approved the final manuscript.

Funding This research was funded by Ferdowsi University of Mashhad under the grant number 3/60492.

Data availability and code availability All data generated or analysed during this study are included in this published article [and its supplementary information files].

Declarations

Competing interests The authors declare that they have no known competing financial interests or personal relationships that could have appeared to influence the work reported in this paper.

Ethics, consent to participate, and consent to publish declarations Not applicable.

Open Access This article is licensed under a Creative Commons Attribution-NonCommercial-NoDerivatives 4.0 International License, which permits any non-commercial use, sharing, distribution and reproduction in any medium or format, as long as you give appropriate credit to the original author(s) and the source, provide a link to the Creative Commons licence, and indicate if you modified the licensed material. You do not have permission under this licence to share adapted material derived from this article or parts of it. The images or other third party material in this article are included in the article's Creative Commons licence, unless indicated otherwise in a credit line to the material. If material is not included in the article's Creative Commons licence and your intended use is not permitted by statutory regulation or exceeds the permitted use, you will need to obtain permission directly from the copyright holder. To view a copy of this licence, visit http://creativeco mmons.org/licenses/by-nc-nd/4.0/.

References

- 1. Chan SHS, Wu TY, Juan JC, Yang C. Recent developments of metal oxide semiconductors as photocatalysts in advanced oxidation processes (AOPs) for treatment of dye waste-water. J Chem Technol Biotechnol. 2011;86(9):1130. https://doi.org/10.1002/jctb.2636.
- Verbeke R, Gomez V, Ivo FJV. Prog Polym Sci. 2017;72:1-15. https://doi.org/10.1016/j.progpolymsci.2017.05.003.
- Kang G-D, Cao Y-M. Development of antifouling reverse osmosis membranes for water treatment: A review. Water Res. 2012;46(3):584– 600. https://doi.org/10.1016/j.watres.2011.11.041.
- 4. Greenlee LF, Lawler DF, Freeman BD, Marrot B, Moulin P. Reverse osmosis desalination: water sources, technology, and today's challenges. Water Res. 2009;43(9):2317-48. https://doi.org/10.1016/j.watres.2009.03.010.
- 5. Duan J, Niu A, Shi D, Wilson F, Graham NJD. Factors affecting the coagulation of seawater by ferric chloride. Desalin Water Treat. 2009;11:173-83. https://doi.org/10.5004/dwt.2009.795.



(2025) 5:83

- Pendergast MTM, Hoek EMV. A review of water treatment membrane nanotechnologies. Energy Environ Sci. 2011;4(6):1946–71. https://doi.org/10.1039/C0EE00541J.
- 7. Han Y, Xu Z, Gao C. Ultrathin graphene nanofiltration membrane for water purification. Adv Funct Mater. 2013;23(29):3693–700. https://doi.org/10.1002/adfm.201202601.
- 8. Kabeel AE, El-Agouz SA. Review of researches and developments on solar stills. Desalination. 2011;276(1–3):1–12. https://doi.org/10. 1016/i.desal.2011.03.042.
- 9. Deng Z, Zhou J, Miao L, Liu C, Peng Y, Sun L, Tanemura S. The emergence of solar thermal utilization: solar-driven steam generation. J Mater Chem A. 2017;5(17):7691–709. https://doi.org/10.1039/C7TA01361B.
- 10. Adham S, Hussain A, Matar JM, Dores R, Janson A. Application of membrane distillation for desalting brines from thermal desalination plants. Desalination. 2013;314:101–8. https://doi.org/10.1016/j.desal.2013.01.003.
- 11. Hussain A, Janson A, Matar JM, Adham S. Membrane distillation: recent technological developments and advancements in membrane materials. Emergent Mater. 2022;5(2):347–67. https://doi.org/10.1007/s42247-020-00152-8.
- 12. He S, Chen C, Kuang Y, Mi R, Liu Y, PeiKong YW, et al. Nature-inspired salt resistant bimodal porous solar evaporator for efficient and stable water desalination. Energy Environ Sci. 2019;12(5):1558–67. https://doi.org/10.1039/C9EE00945K.
- 13. Yu Z, Cheng S, Ruonan Gu, Li Y, Dai S, Mao Z. Interfacial solar evaporator for clean water production and beyond: From design to application. Appl Energy. 2021;299: 117317. https://doi.org/10.1016/j.apenergy.2021.117317.
- Bae K, Kang G, Cho SK, Park W, Kim K, Padilla WJ. Flexible thin-film black gold membranes with ultrabroadband plasmonic nanofocusing for efficient solar vapour generation. J Padilla Nat Commun. 2015;6(1):10103. https://doi.org/10.1038/ncomms10103.
- Li X, Zhang W, Liu Na, Ruixiang Qu, Wei Y, Feng L. Superwetting copper meshes based on self-organized robust CuO nanorods: efficient water purification for in situ oil removal and visible light photodegradation. Nanoscale. 2018;10(9):4561–9. https://doi.org/10.1039/ C7NR09201F.
- 16. Zhao Q, Cui Du, Jia Y, Yuan J, Song G, Zhou X, Sun S, Zhou C, Zhao L, Yang S. Solar-powered Janus membrane for one-step conversion of sewage to clean water. Chem Eng J. 2020;387:124131. https://doi.org/10.1016/j.cej.2020.124131.
- 17. Wang Y, Zhang L, Wang P. Self-floating carbon nanotube membrane on macroporous silica substrate for highly efficient solar-driven interfacial water evaporation. ACS Sustain Chem Eng. 2016;4(3):1223–30. https://doi.org/10.1021/acssuschemeng.5b01274.
- Han S, Yang J, Li X, Li W, Zhang X, Koratkar N, Yu Z-Z. Flame Synthesis of Superhydrophilic Carbon Nanotubes/Ni Foam Decorated with Fe₂O₃ Nanoparticles for Water Purification via Solar Steam Generation. ACS Appl Mater Interfaces. 2020;12(11):13229–38. https://doi.org/ 10.1021/acsami.0c00606.
- 19. Liu H, Chen C, Wen H, Guo R, Williams NA, Wang B, Chen F, Hu L. Narrow bandgap semiconductor decorated wood membrane for high-efficiency solar-assisted water purification. J Mater Chem A. 2018;6(39):18839–13238. https://doi.org/10.1039/C8TA05924A.
- 20. Yao H, Zhang P, Huang Y, Cheng H, Li C, Qu L. Highly efficient clean water production from contaminated air with a wide humidity range. Adv Mater. 2020;32(6):1905875. https://doi.org/10.1002/adma.201905875.
- 21. Ren H, Tang M, Guan B, Wang K, Yang J, Wang F, Wang M, et al. Hierarchical graphene foam for efficient omnidirectional solar–thermal energy conversion. Adv Mater. 2017;29(38):1702590. https://doi.org/10.1002/adma.201702590.
- 22. Cui L, Zhang P, Xiao Y, Liang Y, Liang H, Cheng Z, Qu L. High rate production of clean water based on the combined photo-electro-thermal effect of graphene architecture. Adv mater. 2018;30(22):1706805. https://doi.org/10.1002/adma.201706805.
- 23. Li Y, Gao T, Yang Z, Chen C, Kuang Y, Song J, Jia C, Hitz EM, Yang B, Hu L. Graphene oxide-based evaporator with one-dimensional water transport enabling high-efficiency solar desalination. Nano Energy. 2017;41:201–9. https://doi.org/10.1016/j.nanoen.2017.09.034.
- 24. Han Q, Chen N, Zhang J, Qu L. Mater Horiz. 2017;4(5):832-50. https://doi.org/10.1039/C7MH00379J.
- 25. Lee KM, Lai CW, Ngai KS, Juan JC. Recent developments of zinc oxide based photocatalyst in water treatment technology: a review. Water Res. 2016;88:428–48. https://doi.org/10.1016/j.watres.2015.09.045.
- Cho Y-J, Kim H-I, Lee S, Choi W. Dual-functional photocatalysis using a ternary hybrid of TiO₂ modified with graphene oxide along with Pt and fluoride for H2-producing water treatment. J Catal. 2015;330:387–95. https://doi.org/10.1016/j.jcat.2015.07.007.
- 27. Rajivgandhi GN, Ramachandran G, Kanisha CC, Alharbi NS, Kadaikunnan S, Khaled JM, Alanzi KF, Li W-J. Effect of Ti and Cu doping on the structural, optical, morphological and anti-bacterial properties of nickel ferrite nanoparticles. Results Phys. 2021;23:104065. https://doi.org/10.1016/j.rinp.2021.104065.
- 28. Shokri S, Shariatifar N, Molaee-Aghaee E, Khaniki GJ, Sadighara P, Faramarzi MA, Mohammadi M, Rezagholizade-Shirvan A. Synthesis and characterization of a novel magnetic chitosan–nickel ferrite nanocomposite for antibacterial and antioxidant properties. Sci Rep. 2023;13(1):15777. https://doi.org/10.1038/s41598-023-42974-6.
- 29. Praveena MG, Mohammed EM. Tailoring the structural, morphological, optical, cytotoxicity, and antibacterial properties of low temperature calcined nickel ferrite nanoparticles. J Solgel Sci Technol. 2021;100:496–505. https://doi.org/10.1007/s10971-021-05660-5.
- 30. Kocijan M, Ćurković L, Gonçalves G, Podlogar M. The Potential of rGO@TiO₂ Photocatalyst for the Degradation of Organic Pollutants in Water. Sustainability. 2022;14(19):12703. https://doi.org/10.3390/su141912703.
- 31. Lin W, Xie X, Wang X, Wang Y, Segets D, Sun J. Efficient adsorption and sustainable degradation of gaseous acetaldehyde and o-xylene using rGO-TiO₂ photocatalyst. Chem Eng J. 2018;349:708–18. https://doi.org/10.1016/j.cej.2018.05.107.
- 32. Afzal MJ, Pervaiz E, Farrukh S, Ahmed T, Bingxue Z, Yang M. Highly integrated nanocomposites of RGO/TiO₂ nanotubes for enhanced removal of microbes from water. Environ Technol. 2018. https://doi.org/10.1080/09593330.2018.1447021.
- 33. Ruidíaz-Martínez M, Álvarez MA, López-Ramón MV, Cruz-Quesada G, Rivera-Utrilla J, Sánchez-Polo M. Catalysts. 2020;10(5):520. https://doi.org/10.3390/catal10050520.
- 34. Rodríguez V, Camarillo R, Martínez F, Jiménez C, Rincón J. High-pressure synthesis of rGO/TiO₂ and rGO/TiO₂/Cu catalysts for efficient CO₂ reduction under solar light. J Supercrit Fluids. 2021;174:105265. https://doi.org/10.1016/j.supflu.2021.105265.
- 35. Andreozzi M, Álvarez MG, Contreras S, Medina F, Clarizia L, Vitiello G, Llorca J, Marotta R. Treatment of saline produced water through photocatalysis using rGO-TiO₂ nanocomposites. Catal Today. 2018;315:194–204. https://doi.org/10.1016/j.cattod.2018.04.048.
- 36. Nisar A, Saeed M, Muneer M, Üsman M, Khan I. Synthesis and characterization of ZnO decorated reduced graphene oxide (ZnO-rGO) and evaluation of its photocatalytic activity toward photodegradation of methylene blue. Environ Sci Pollut. 2022. https://doi.org/10.1007/s11356-021-13520-6.



- 37. Sengunthar P, Bhavsar KH, Balasubramanian C, Joshi US. Physical properties and enhanced photocatalytic activity of ZnO-rGO nanocomposites. Appl Phys A. 2020;126(7):567. https://doi.org/10.1007/s00339-020-03753-6.
- 38. Gulati A, Malik J, Kakkar R. Mesoporous rGO@ ZnO composite: Facile synthesis and excellent water treatment performance by pesticide adsorption and catalytic oxidative dye degradation. Chem Eng Res Des. 2020;160:254–63. https://doi.org/10.1016/j.cherd.2020.04.040.
- 39. Pang YL, Tee SF, Lim S, Abdullah AZ, Ong HC, Wu CH, Chong WC, Mohammadu AW, Mahmoudi E. Enhancement of photocatalytic degradation of organic dyes using ZnO decorated on reduced graphene oxide (rGO). Desalin Water Treat. 2018;108:311–21. https://doi.org/10.5004/dwt.2018.21947.
- 40. Van Bao H, Dat NM, Giang NTH, Thinh DB, Trinh DN, Hai ND, Khoa NAD, Nam HM, Phong MT, Hieu NH. Behavior of ZnO-doped TiO₂/rGO nanocomposite for water treatment enhancement. Surf Interfaces. 2021;23:100950. https://doi.org/10.1016/j.surfin.2021.100950.
- 41. He G, Wen Y, Ma C, Li X, Gao L, Sun Z. Photocatalytic hydrogen evolution of nanoporous CoFe₂O₄ and NiFe₂O₄ for water splitting. Int J Hydrog Energy. 2021;46(7):5369–77. https://doi.org/10.1016/j.ijhydene.2020.11.107.
- 42. Sakhare PA, Pawar SS, Bhat TS, Yadav SD, Patil GR, Patil PS, Sheikh AD. Magnetically recoverable BiVO4/NiFe2O4 nanocomposite photocatalyst for efficient detoxification of polluted water under collected sunlight. Mater Res Bull. 2020. https://doi.org/10.1016/j.materresbull.2020.110908.
- 43. Kalita C, Boruah PK, Das MR, Saikia P. Facile green synthesis of nickel-ferrite-rGO (NiFe₂O₄/rGO) nanocomposites for efficient water purification under direct sunlight. Inorg Chem Commun. 2022;146:110073. https://doi.org/10.1016/j.inoche.2022.110073.
- 44. Jihad KM, Roknabadi MR, Mohammadi M, Goharshadi EK. Reduced graphene oxide/TiO₂/NiFe₂O₄ nanocomposite as a stable photocatalyst and strong antibacterial agent. Sustain Environ Res. 2023;33:43. https://doi.org/10.1186/s42834-023-00200-y.
- 45. Abdi Z, Khachatourian AM, Nemati A. Visible-light-driven photocatalytic activity of NiFe₂O₄@ Ti-doped ZnO magnetically separable nanoparticles anchored on N-doped rGO nanosheets. Diam Relat Mater. 2023;135:109839. https://doi.org/10.1016/j.diamond.2023.109839.
- 46. Atashi FSS, Heshmatpour F. TiO₂/NiFe_{2-x}Ce_xO₄/rGO ternary magnetic nanocomposite as separable and recyclable photocatalyst. Inorg Chem Commun. 2025;171:113603. https://doi.org/10.1016/j.inoche.2024.113603.
- 47. Farzaneh A, Saghatoleslami N, Goharshadi EK, Gharibi H, Ahmadzadeh H. 3-D mesoporous nitrogen-doped reduced graphene oxide as an efficient metal-free electrocatalyst for oxygen reduction reaction in alkaline fuel cells: Role of π and lone pair electrons. Electrochim Acta. 2016;222:608–18. https://doi.org/10.1016/j.electacta.2016.11.015.
- 48. Abed M, Roknabadi MR, Pour AN. Improvement of physical properties of zinc oxide and activated carbon nanocomposite for use in supercapacitor electrode. J Mater Sci Mater Electron. 2024;35:1328. https://doi.org/10.1007/s10854-024-12961-2.
- 49. Aziznezhad M, Goharshadi E, Namayandeh-Jorabchi M. Surfactant-mediated prepared VO₂ (M) nanoparticles for efficient solar steam generation. Sol Energy Mater Sol Cells. 2020;211:110515. https://doi.org/10.1016/j.solmat.2020.110515.
- 50. Mbrouk O, Fawzy M, El-Shafey HM, Saif M, Abdel-Mottaleb MSA, Hafez H. Viable production of hydrogen and methane from polluted water using eco-friendly plasmonic Pd–TiO 2 nanocomposites. RSC Adv. 2023;13:770–80. https://doi.org/10.1039/D2RA07442G.
- 51. Mbrouk O, Hafez H, Mozia S, Othman AM, Abdel Mottaleb MSA. Stimulated generation of photobiogas by morphologically tuned nano-structured ZnO and ZnO/TiO₂. BMC Chem. 2022;16:74. https://doi.org/10.1186/s13065-022-00866-2.
- 52. Rono N, Kibet JK, Martincigh BS, Nyamori VO. A comparative study between thermal etching and liquid exfoliation of bulk graphitic carbon nitride to nanosheets for the photocatalytic degradation of a model environmental pollutant, Rhodamine B. J Mater Sci Mater Electron. 2021;32:687–706. https://doi.org/10.1007/s10854-020-04849-8.
- 53. Siburian R, Sihotang H, Lumban Raja S, Supeno M, Simanjuntak C. New route to synthesize of graphene nano sheets. Orient J Chem. 2018;34(1):182. https://doi.org/10.13005/ojc/340120.
- 54. Kumar A, Sadanandhan AM, Jain SL. Retracted Article: Silver doped reduced graphene oxide as a promising plasmonic photocatalyst for oxidative coupling of benzylamines under visible light irradiation. New J Chem. 2019;43(23):9116–22. https://doi.org/10.1039/C9NJ0 0852G.
- 55. Elias Uddin Md, Kim NH, Kuila T, Lee SH, Hui D, Lee JH. Preparation of reduced graphene oxide-NiFe2O4 nanocomposites for the electrocatalytic oxidation of hydrazine. Compos B Eng. 2015;79:649–59. https://doi.org/10.1016/j.compositesb.2015.05.029.
- 56. Sun L, Zhao Z, Zhou Y, Liu Li. Anatase TiO₂ nanocrystals with exposed {001} facets on graphene sheets via molecular grafting for enhanced photocatalytic activity. Nanoscale. 2012;4(2):613–20. https://doi.org/10.1039/C1NR11411E.
- 57. Mohammadi M, Roknabadi MR, Behdani M, Kompany A. Enhancement of visible and UV light photocatalytic activity of rGO-TiO2 nano-composites: The effect of TiO₂/Graphene oxide weight ratio. Ceram Int. 2019;45(10):12625–34. https://doi.org/10.1016/j.ceramint.2019.02.129.
- 58. Sethi M, Sandhya Shenoy U, Muthu S, Krishna Bhat D. Facile solvothermal synthesis of NiFe₂O₄ nanoparticles for high-performance supercapacitor applications. Front Mater Sci. 2020;14:120–32. https://doi.org/10.1007/s11706-020-0499-3.
- 59. Xie Z, Duo Y, Lin Z, Fan T, Xing C, Yu L, Wang R, et al. Adv Sci. 2020;7(5):1902236. https://doi.org/10.1002/advs.201902236.
- Hema E, Manikandan A, Karthika P, Arul Antony S, Venkatraman BR. A Novel Synthesis of Zn²⁺-Doped CoFe₂O₄ Spinel Nanoparticles: Structural, Morphological, Opto-magnetic and Catalytic Properties. J Supercond Nov Magn. 2015;28:2539–52. https://doi.org/10.1007/s10948-015-3054-1.
- 61. Mahdikhah V, Saadatkia S, Sheibani S, Ataie A. Outstanding photocatalytic activity of CoFe₂O₄/rGO nanocomposite in degradation of organic dyes. Opt Mater. 2020;108: 110193. https://doi.org/10.1016/j.optmat.2020.110193.
- 62. World Health Organization. Guidelines for drinking water quality, 4th edn. World Health Organization; 2011, p. 307.
- 63. Zhu M, Yu J, Ma C, Zhang C, Wu D, Zhu H. Carbonized daikon for high efficient solar steam generation. Sol Energy Mater Sol Cells. 2019;191:83–90. https://doi.org/10.1016/j.solmat.2018.11.015.

Publisher's Note Springer Nature remains neutral with regard to jurisdictional claims in published maps and institutional affiliations.

